



HAL
open science

Influence of composition of nuclear waste glasses on vapor phase hydration

Sathya Narayanasamy, Patrick Jollivet, Nicole Godon, Frédéric Angeli, S. Gin,
Martiane Cabié, Julien Cambedouzou, Corentin Le Guillou, Abdesselam
Abdelouas

► **To cite this version:**

Sathya Narayanasamy, Patrick Jollivet, Nicole Godon, Frédéric Angeli, S. Gin, et al.. Influence of composition of nuclear waste glasses on vapor phase hydration. *Journal of Nuclear Materials*, 2019, *Journal of Nuclear Materials*, pp.53-71. 10.1016/j.jnucmat.2019.07.015 . hal-02277978

HAL Id: hal-02277978

<https://hal.univ-lille.fr/hal-02277978v1>

Submitted on 27 Sep 2019

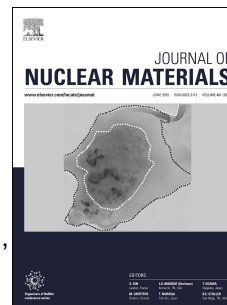
HAL is a multi-disciplinary open access archive for the deposit and dissemination of scientific research documents, whether they are published or not. The documents may come from teaching and research institutions in France or abroad, or from public or private research centers.

L'archive ouverte pluridisciplinaire **HAL**, est destinée au dépôt et à la diffusion de documents scientifiques de niveau recherche, publiés ou non, émanant des établissements d'enseignement et de recherche français ou étrangers, des laboratoires publics ou privés.

Accepted Manuscript

Influence of composition of nuclear waste glasses on vapor phase hydration

Sathya Narayanasamy, Patrick Jollivet, Nicole Godon, Frédéric Angeli, Stéphane Gin, Martiane Cabié, Julien Cambedouzou, Corentin Le Guillou, Abdesselam Abdelouas



PII: S0022-3115(19)30397-6

DOI: <https://doi.org/10.1016/j.jnucmat.2019.07.015>

Reference: NUMA 51715

To appear in: *Journal of Nuclear Materials*

Received Date: 1 April 2019

Revised Date: 12 July 2019

Accepted Date: 14 July 2019

Please cite this article as: S. Narayanasamy, P. Jollivet, N. Godon, Fréé. Angeli, Sté. Gin, M. Cabié, J. Cambedouzou, C. Le Guillou, A. Abdelouas, Influence of composition of nuclear waste glasses on vapor phase hydration, *Journal of Nuclear Materials* (2019), doi: <https://doi.org/10.1016/j.jnucmat.2019.07.015>.

This is a PDF file of an unedited manuscript that has been accepted for publication. As a service to our customers we are providing this early version of the manuscript. The manuscript will undergo copyediting, typesetting, and review of the resulting proof before it is published in its final form. Please note that during the production process errors may be discovered which could affect the content, and all legal disclaimers that apply to the journal pertain.

1 Influence of composition of nuclear waste glasses on vapor phase hydration

2 Sathya Narayanasamy^a, Patrick Jollivet^a, Nicole Godon^a, Frédéric Angeli^a, Stéphane Gin^a, Martiane Cabié^b,
3 Julien Cambedouzou^{c,d}, Corentin Le Guillou^e, Abdesselam Abdelouas^f

4 ^a CEA Marcoule, DEN, MAR, DE2D, SEVT/LCLT, bât 208, BP17171, 30207 Bagnols sur Cèze cedex, France

5 ^b Aix Marseille Univ, CNRS, Centrale Marseille, FSCM, CP2M, Marseille France

6 ^c ICSM, CEA, CNRS, ENSCM, Univ. Montpellier, Marcoule, France

7 ^d IEM, CNRS, ENSCM, Univ. Montpellier, Montpellier, France

8 ^e UMET-Unité Matériaux et Transformations, CNRS UMR 8207, Université de Lille, 59655 Villeneuve
9 d'Ascq, France

10 ^f SUBATECH, CNRS-IN2P3, IMT Atlantique-Université de Nantes, 4 rue Alfred Kastler, BP 20722, 44307
11 Nantes cedex 03, France

12 Abstract

13 For the first time, the influence of glass composition on the vapor hydration kinetics of the French AVM
14 nuclear waste glass simulants was investigated. Three complex borosilicate glasses (> 20 oxides) along
15 with three simplified Na/(Ca, Na)/(Mg, Na)-alumino-borosilicate glasses with four or five oxides were
16 altered at 50°C in water vapor (95% RH) for up to 557 days. The solid characterization of the altered
17 samples (by SEM, TEM, XRD, ToF-SIMS, SAXS) revealed that the rate-controlling vapor hydration
18 mechanism is composition dependent. The vapor hydration rate of the more durable glasses, whose
19 molar ratio of Al₂O₃/(CaO or MgO) is ≥1, seems to be limited by network-hydrolysis, whereas the overall
20 glass alteration rate of the less durable glasses, whose Al₂O₃/MgO ratio is <1, seems to be driven by the
21 precipitation of Mg-rich secondary phases. All the vapor hydrated glasses show the presence of a
22 homogeneous gel layer of a few tens of nm thickness. The more durable glasses have a smaller quantity
23 of secondary phases precipitated on their surface. The less durable glasses have a relatively significant
24 quantity of secondary phases precipitated above the gel layer and irregularly shaped, scattered and
25 highly porous altered zones formed beneath the gel layer. The overall alteration rate of the less durable
26 glasses was 10-20 times faster than the more durable glasses. For all glasses, FTIR spectroscopy indicated
27 an inflexion in the vapor hydration rate after 120-200 days of alteration, likely due to a passivating effect
28 of the altered layer formed under unsaturated conditions. The average pore size of the altered layer in

29 certain vapor hydrated glasses measured by SAXS is similar to the pore sizes of the gel layer formed in
30 aqueous medium and varies very slightly with glass composition.

31 1. Introduction

32 The high-level activity radioactive waste (HLW), issued from the nuclear power industry, is immobilized
33 in a vitreous matrix, since glass has been proven to be a stable solid form for thousands of years based
34 on archeological or geological evidence [1, 2]. According to the permanent nuclear waste disposal
35 solution envisaged by ANDRA (the French national radioactive waste management agency), the waste
36 glass packages (glass in a stainless steel canister encased in a low-alloy steel overpack) will be stored in
37 an underground repository constructed with steel and concrete reinforcements in clay layer 500 m
38 beneath the earth's surface. The steel corrosion in the closed underground repository would result in
39 hydrogen gas liberation. As a result, the re-saturation of the site with ground water from the surrounding
40 clay medium will be slowed down. Consequently, it is expected that nuclear waste glasses maybe
41 exposed to an unsaturated medium for up to tens of thousands of years before being completely
42 immersed in aqueous ground water [3]. Therefore it is mandatory to investigate the consequences of
43 glass alteration in vapor phase, the mechanisms involved and the influence of intrinsic and extrinsic
44 parameters [4]. Glass alteration in vapor phase has been relatively less studied in comparison to
45 alteration in aqueous medium [5-15].

46 Vapor hydration experiments on a variety of nuclear waste glasses and their non-radioactive surrogates
47 have been conducted by different laboratories in USA [16-26], UK [27] and France [28-33]. From the
48 experimental results so far, it can be understood that the reactions occurring between glass and water
49 are the same for alteration in aqueous medium and unsaturated water vapor. However, the rate
50 controlling reaction mechanism and the driving force for alteration are different in both cases. The
51 difference arises largely due to the very small volume of water in vapor phase and almost no leaching by
52 solution, unless water condenses and flows away from the altered surface. The precipitation of
53 secondary phases seems to be the strongest driving force for alteration in vapor phase at high
54 temperature. A majority of the vapor hydration studies conducted so far have been done in extreme
55 conditions (150-200°C & 100% relative humidity (RH)) favorable for secondary phases precipitation. This
56 temperature range is not representative of the expected scenario in the French geological disposal
57 facility. It is expected that the temperature of the waste glass packages will be lower than or equal to
58 50°C [34]. The vapor hydration of SON68 (French inactive reference nuclear waste glass) at high
59 temperatures (90-200°C, activation energy (E_a)=43-47 KJ/mol) [28] and lower temperatures (35-90°C,

60 $E_a=34\pm 0.4$ KJ/mol) [31] suggests that the rate-controlling mechanisms may depend on temperature. The
61 limited data of the studies have also confirmed the influence of relative humidity [16], glass composition
62 [22, 27, 35-37], composition of the vapor phase [30] and radioactivity [38] on vapor hydration kinetics.
63 Insights on glass alteration in vapor phase can also be obtained from studies on atmospheric alteration
64 of window glasses, art crafts, stained-glass windows of historic sites etc. [39-41]. Almost all these studies
65 have shown similar altered layer morphology on the glass surface in contact with an unsaturated
66 medium. An altered layer, commonly referred to as 'gel layer', is formed adjacent to pristine glass. This
67 gel layer has been suggested to be formed by mechanisms of hydration (penetration of water molecules)
68 [37] / inter-diffusion ($(\equiv Si - O^- M^+)_{glass} + H_{water}^+ \rightarrow (\equiv Si - OH)_{glass} + M_{water}^+$) [40, 42] / network
69 hydrolysis ($(\equiv Si - O - Si \equiv)_{glass} + H_2O \rightarrow 2 (\equiv Si - OH)_{glass}$) [31, 43, 44] or a combination of
70 these mechanisms [39, 41]. Localized dissolution-precipitation or condensation mechanisms and re-
71 organization of the gel layer have also been discussed in literature [31, 39]. On the surface of this gel
72 layer, amorphous / crystalline secondary precipitates maybe present [23, 31, 36]. In certain cases, the
73 secondary phases may also accelerate the vapor hydration kinetics [22].

74 In this article, the focus is on the influence of glass composition on vapor hydration. Through literature
75 survey, it can be understood that glass composition can affect glass durability in three ways. (i) The
76 presence of alkaline elements in the glass can promote the quantity of water adsorbed on surface,
77 facilitate inter-diffusion mechanism and may result in increased hydration rate [22, 37, 45]. (ii) Glass
78 composition plays an important role in the precipitation of secondary phases under given conditions and
79 thus may accelerate glass alteration [22, 35]. (iii) Presence of elements such as Zn, which increases the
80 resistance to network hydrolysis, may increase glass durability in vapor phase [27]. The literature study
81 led us to understand that certain elements such as Al may have a dual role depending on whether the
82 conditions are favorable for secondary phase precipitation (negative effect) or if they participate in
83 increasing the resistance of glass network to hydrolysis (positive effect). Therefore, the temperature of
84 the experiments needs to be carefully chosen, as the influence of the glass composition on its alteration
85 could vary with temperature.

86 In this study, the influence of nuclear waste glass composition on vapor hydration has been investigated
87 by studying the behavior of three AVM (*Atelier de Vitrification de Marcoule*) glasses in contact with water
88 vapor. The AVM glasses are complex borosilicate glasses containing more than 20 oxides including fission
89 products issued from the UNGG (*Uranium Naturel Graphite-Gaz*) reactor at Marcoule. The range in the
90 AVM glasses composition is extensive due to the variation in the composition of fission products

91 solution. The long-term behavior of these HLW radioactive glasses in aqueous media was studied using
92 many inactive surrogates [46, 47]. Based on this study, the glasses AVM6, AVM10 and AVMV4 are the
93 three inactive surrogates selected for the current study. AVM6 is known to alter at the highest residual
94 rate (r_r) in deionized water at 50°C and AVM10 alters at the lowest r_r . AVMV4 is a simulant of the actual
95 composition of the HLW glass produced at Marcoule facility.

96 The specific influence of alkaline-earth elements such as Mg and Ca was investigated, since AVM glasses
97 contain a significant amount of Mg and very little Ca and the effects of these elements on glass alteration
98 rate in aqueous medium are relatively well-known [48-52]. Based on literature review, it is expected that
99 these elements would be detrimental to glass durability in unsaturated medium due to their tendency to
100 form secondary precipitates. The study of their specific influence cannot be carried out using a complex
101 glass with several oxides due to possible interference and synergies between other elements. Therefore,
102 three simplified glasses (Q, QCa and QMg) were prepared based on the Si/Al stoichiometry of AVMV4.
103 The use of simplified glass compositions helps to understand the role of specific element on glass
104 durability [53-56].

105 The fission products loading of AVM glasses suggests that the temperature of the glass packages during
106 the expected time of exposure to water vapor will be around 50°C. Therefore, it was decided to conduct
107 our experiments at 50°C. It is suspected that the rate-controlling vapor hydration mechanisms may vary
108 with conditions favorable for precipitations of certain silica-rich secondary phases at higher
109 temperatures (>90°C). The relative humidity (RH) was chosen to be 95% since the conditions expected in
110 the repository are close to saturation [34].

111 2. Materials and methods

112 2.1 Sample preparation

113 The synthesis of the AVM glasses has already been described by Thien [46]. The glass samples for this
114 study were retrieved from the same batch. Q, QCa and QMg were prepared using the oxide precursors
115 (SiO_2 , H_3BO_3 , Na_2CO_3 , Al_2O_3 , CaO (for QCa) and MgO (for QMg)). The mixtures were put in a Pt-Rh
116 crucible and heated during 3 h at 1450°C. They were then annealed at 620°C during 1 h in a graphite
117 crucible. Afterwards, the temperature of the furnace was decreased at a rate of 0.5°C/min until 300°C
118 and then it was turned off. The compositions of the glasses after dissolution in acid solution were
119 determined by Inductively Coupled Plasma-Optical Emission Spectroscopy (ICP-OES). The data in mol%
120 oxides are provided in table 1. The error percentage associated with the measured values is 3%. The

121 fraction of Non-Bridging Oxygen (NBO) atoms in the glass network was theoretically calculated based on
 122 equation 2.1.1 and equation 2.1.2. ¹¹B NMR spectra (not presented here) were collected on a Bruker
 123 Avance II 500WB spectrometer. The calculated NBO values and the fraction of B^(IV) for each glass are
 124 provided in table 1. The error associated varies between 3 to 8%.

$$125 \quad NBO = \frac{2 * (\text{mol fr. of oxides of modifier cations} - \text{mol fr. of oxides of network former requiring charge compensation})}{N(O)} \quad \text{Equation 2.1.1}$$

$$126 \quad N(O) = \sum(\text{no. of oxygen atoms in 1 molecule of oxide} * \text{mol fr. of oxide}) \quad \text{Equation 2.1.2}$$

127 For all glasses, the NBO values are similar despite their differences in compositions (except Q). The
 128 percentage of B^(IV) in each glass shows that Mg is less efficient to compensate [BO₄]⁻ entities than Ca.

129
 130 For each glass, two monoliths of dimensions (2.5x2.5x0.1 cm³) were prepared for vapor hydration during
 131 180 days and 557 days, respectively. These monoliths were cut from the glass bars and polished to
 132 optical finish (surface roughness <<1 μm) on both faces. Similarly, one polished monolith for each glass
 133 was also prepared with dimensions (2.5x2.5x0.08 cm³) for the purpose of studying hydration kinetics
 134 using Fourier Transform Infrared (FTIR) spectroscopy. All the glass monoliths were washed in ultra-pure
 135 acetone and absolute ethanol under ultrasonic agitation and dried for a few hours in an oven at 50°C
 136 before starting the experiment. Powder samples of each glass were prepared by crushing glass pieces
 137 using Retsch MM400 ball-mill apparatus equipped with tungsten carbide balls. The size fraction of 2 – 5
 138 μm were separated using pure acetone solvent and the application of Stokes law, for Small Angle X-ray
 139 Scattering (SAXS) measurement.

140 **2.2 Alteration Protocol**

141 A WEISS WKL64 climatic chamber was used to hydrate the samples at 50°C and 95% RH. The apparatus
 142 continuously monitors and displays the temperature and RH in the test zone. De-mineralized water is
 143 used to produce steam and then de-humidified to have the programmed RH in the test zone. The
 144 monolithic glass samples are placed horizontally in a curved grid Teflon basket that allows the sample to
 145 be exposed to vapor on both faces. The glass powders were dispersed in plastic petri dishes. Similar
 146 protocol for vapor hydration of glasses has been used before in literature [39].

147 **2.3 Experiments**

148 **2.3.1 Hydration kinetics**

149 A glass monolith of dimensions ($2.5 \times 2.5 \times 0.08 \text{ cm}^3$) was placed in the climatic chamber at 50°C and 95%
150 RH. The sample was removed periodically (approximately once a month) for a short duration (~ 10
151 minutes) and analyzed in transmission mode using a Vertex 70 FTIR spectrometer. It was then replaced
152 in the chamber to continue hydration. Five spectra at different regions of the monolith were recorded
153 and averaged. The diameter of the diaphragm was set to 6 mm. The spectra were recorded from 4000 to
154 400 cm^{-1} . The deconvolution of the spectra from 4000 to 2600 cm^{-1} into five Gaussian bands was
155 attributed to the vibration of the OH stretching mode in SiOH molecules ($\sim 3595\text{-}3605 \text{ cm}^{-1}$), bound
156 water-silanol groups ($\sim 3515\text{-}3518 \text{ cm}^{-1}$ & $\sim 3170\text{-}3185 \text{ cm}^{-1}$), symmetrical OH stretching mode in the free
157 water molecule ($\sim 3400\text{-}3415 \text{ cm}^{-1}$) and the glass matrix ($\sim 2700 \text{ cm}^{-1}$). This type of deconvolution is based
158 on the protocol used to follow vapor hydration kinetics using infrared spectroscopy in recent literature
159 [29, 32, 57, 58]. The hydration kinetics was followed by studying the evolution of the increase in
160 absorbance of the band attributed to the OH stretching mode in SiOH molecules over time.

161 Calculation of error in the increase in absorbance values: With every deconvolution, the standard error
162 associated with the increase in the area of the Gaussian is calculated by Origin software. The error values
163 for the Gaussian fit are less than 2%. However, while measuring the FTIR spectrum at 5 different places
164 for the same sample, the sample compartment is opened and closed. Due to this the background that
165 was earlier measured is disturbed. Therefore, several backgrounds were measured throughout the day
166 of the FTIR analysis, and the standard deviation among the absorbance values in the range of
167 wavenumbers $3595\text{-}3605 \text{ cm}^{-1}$ was used to calculate the error value. After error propagation calculation,
168 0.02 (a.u.) was calculated as the error value.

169 **2.3.2 Characterization of altered glasses**

170 For each composition, two glass monoliths of dimensions ($2.5 \times 2.5 \times 0.1 \text{ cm}^3$) and the glass powders
171 were placed in the climatic chamber at 50°C and 95% RH for a period of 180 days and 557 days
172 respectively. Afterwards, the monoliths were removed from the chamber and cut into dimensions of
173 ($1 \times 1 \times 0.1 \text{ cm}^3$) approximately for characterization by Scanning Electron Microscope (SEM), Transmission
174 Electron Microscope (TEM), X-Ray Diffraction (XRD) and Time-of-Flight Secondary Ion Mass Spectrometry
175 (ToF-SIMS). The glass powders were characterized by Small Angle X-ray Scattering (SAXS) to probe the
176 porosity and the pore-size of the gel layer.

177 For the purpose of studying the evolution of pore characteristics of the gel layer with time, the
178 powdered samples of AVM6 were altered for 11 days, 31 days and 90 days at 50°C and 95% RH, in
179 addition to the standard alteration time of 180 days and 557 days. These samples were characterized by
180 SAXS.

181 **2.4 Characterization techniques**

182 **2.4.1 SEM**

183 Morphological analysis of the altered samples were carried out using a field emission Scanning Electron
184 Microscope (SEM) Zeiss Gemini Supra 55, JEOL JSM 6330F with an Energy Dispersive Spectroscopy (EDS)
185 system.

186 **2.4.2 TEM**

187 FEI TECNAI G2 Transmission Electron Microscope (TEM) was used for morphological and chemical
188 analysis. The 80 kV to 200 kV TEM permits to do conventional imaging and analytics, disposes of bright-
189 field and dark-field imaging, EDS and Scanning TEM (STEM) to probe chemical composition of materials.
190 The spatial resolution is 0.27 nm. Ultra-thin samples for observation by TEM (the length of the sample is
191 approx. 5 μm and it is about one hundred nm thick) were prepared using Dual Beam FIB (FEI Helios 600
192 NanoLab). The uncertainty associated with the quantitative STEM-EDX analyses was estimated to be
193 around 12% relative error. Scanning transmission electron microscopy (STEM) and EDS mapping were
194 performed on QMg sample altered for 180 days using a Thermofisher Titan Themis 300 microscope
195 operated at 300 keV, located at the "Centre Commun de Microscopie – CCM" at the university of Lille.
196 Hyperspectral EDS data were obtained using the super-X detector system equipped with four
197 windowless silicon drift detectors. The probe current was set at 50 pA. The analysis of the hyperspectral
198 data was performed using the Hyperspy python-based package [59]. The signal was first denoised using
199 Principal Component Analysis (PCA). Then, the EDS spectra at each pixel were fitted by a series of
200 Gaussian functions and a physical model for background/bremsstrahlung. Quantification was performed
201 thanks to the Cliff-Lorimer method, using experimentally determined k-factors and absorption correction
202 routines.

203 **2.4.3 XRD**

204 Crystalline secondary phases were identified using a Philips X'Pert diffractometer X-Ray Diffraction (XRD)
205 apparatus equipped with a copper tube and a goniometer (4-80° 2 θ , step size 0.01744°). Each glass
206 monolith was analyzed for 12 h on a multiple purpose sample stage (MPSS).

207 **2.4.4 ToF-SIMS**

208 The behavior of elements in the altered layer was characterized using ToF-SIMS (SSIMS on TOF 5
 209 (IONTOF)). Depth profiles of secondary positive ions were obtained by alternating analysis and abrasion
 210 cycles. 25 keV Bi_1^+ primary ions at 2 pA current were used for analysis cycles. 1 keV primary O_2^+ ions at
 211 250 nA current were used for the abrasion cycles. The eroded area was $200 \times 200 \mu\text{m}^2$. The analyzed area
 212 was $60 \times 60 \mu\text{m}^2$ for the samples altered for 180 days and $50 \times 50 \mu\text{m}^2$ for the samples altered for 557 days.
 213 The surface charge was neutralized on the monoliths by a pulsed low-energy (<20 keV) electron flux. The
 214 depth calibration was carried out using the abrasion rate and a mechanical profilometer to measure the
 215 crater depth at the end of the analysis. It is to be noted that the same abrasion rate was used for
 216 analyzing the gel layer and the pristine glass. This choice was justified by the good correspondence
 217 between thickness of altered layer measured by SEM and ToF-SIMS in other works [31].

218 The profiles were normalized with respect to the intensity of each element (C) in the pristine glass
 219 (denoted as PG) and with respect to the intensity of Si (C_{Si}) at given depth as shown in the equation
 220 2.4.4.1 below.

$$221 \quad \text{Normalized intensity} = \frac{\frac{C}{C_{\text{Si}}}}{\left(\frac{C}{C_{\text{Si}}}\right)_{\text{PG}}} \quad \text{Equation 2.4.4.1}$$

$$222 \quad \text{Altered layer depth} = x_0 \text{ at which } \left(0.5 - \frac{\frac{C_B}{C_{\text{Si}}}}{\left(\frac{C_B}{C_{\text{Si}}}\right)_{\text{PG}}} = 0 \right) \quad \text{Equation 2.4.4.2}$$

223 In literature, the most immobile element in the glass network is used for normalization of ToF-SIMS
 224 profiles to avoid matrix effects, which could be either Si or Zr [60, 61]. In our experiments, Si can be
 225 considered immobile. This is valid after verification that Si bearing phases are in relatively small quantity.
 226 It was chosen as the element for normalization since it is present in a sufficiently large quantity in the
 227 glass, such that the precipitation of secondary phases on the glass surface will not result in depletion of a
 228 large fraction of this element.

229 Boron is a good tracer for glass alteration in aqueous medium since it is neither retained in the gel layer
 230 nor forms secondary phases. In vapor phase it would be logical to expect that the retention of boron in
 231 the gel layer is much higher since the quantity of water available to leach boron is highly limited.
 232 However, the ToF-SIMS profiles indicate that the retention of boron in the gel layers is very limited (<
 233 20%). Therefore, boron is used as a tracer to measure altered layer thickness in the vapor hydration

234 phenomenon as well. The thickness of the altered layer was determined based on the profile of boron as
235 shown in equation 2.4.4.2. The thickness of the zone of interface between gel layer and pristine glass
236 measured by ToF-SIMS could be influenced by sample artefacts such as surface roughness of the sample
237 due to precipitates or due to the heterogeneity of the altered layer.

238 **2.4.5 SAXS**

239 The apparatus used is a SAXS-Mo apparatus emitting monochromatic X-ray beam at λ 0.709 Å and the
240 photon flux is 3×10^6 photons.s⁻¹ approximately. The q-range covered is 0.2 to 30 nm⁻¹. The distance scale
241 D is related to the scattering vector q by the formula $D = 2\pi/q$. The sample was filled in a glass capillary
242 tube of 2 mm (e_s) diameter and approximately 10 μm wall thickness. In the section of the sample
243 analyzed, the inter-grain porosity is filled with air. The inner porosity of each grain could be filled with air
244 or water. The data treatment for a porous or granular medium with special attention to the case of glass
245 leaching by water was handled by Spalla et al. 2003 [62]. The data treatment was based on previous
246 works [62-64] and is explained in detail in the supplementary data (section1).

247

248 3. Results

249 The solid characterization of the altered glass has given insights into the morphology of the altered layer,
250 behavior of elements in the altered layer, porosity of the altered layer and the vapor hydration kinetics.
251 In each subsection, the results of all six glasses have been presented. An overall analysis of the results
252 showed that the behavior of the altered glasses AVM6 and AVM10 is similar and that of AVMV4 and
253 QMg is similar. For this reason, the results of these two couples of glasses have been presented together
254 in section 3.1 and section 3.3. The Q and QCa glasses, which do not contain Mg, are also presented
255 following the four above mentioned Mg-containing glasses.

256 **3.1 Morphology of the altered layer (SEM/TEM images)**

257 **3.1.1 AVM6 and AVM10**

258 The SEM images showed that the alteration of these two glasses is similar in the following
259 accounts:

260 (i) Irregular alteration: SEM images of cross-sections showed that both glasses had altered in a
261 heterogeneous manner. Figure 1 shows the SEM and TEM cross-sections of AVM6 and AVM10 altered
262 for 180 days and 557 days (denoted hereafter as AVM6-180, AVM6-557, AVM10-180 and AVM10-557).

263 The altered surface was punctuated with low density altered zones in the shape of irregular cups whose
264 widths and depths varied from a few hundred nm to a few μm (figure 1 (a) and (c) and supplementary
265 data-figure S 1). They were formed on both faces. TEM images of micro-sections showed that in both
266 glasses, these irregular zones were highly porous. This was the case for all four samples. According to
267 STEM-EDX analysis (supplementary data-Section 3, figures S 6, S 7 and S 8), the porous zone is depleted
268 in Mg, Fe and enriched in Ca.

269 An attempt to calculate a statistical average thickness of the altered layer of the AVM10-180
270 sample was made. Ten cross-section SEM images on both faces of AVM10-180 were taken. These images
271 spanned a width of approx. 10 μm each and were taken at a distance of approx. 500 μm apart from one
272 another. From these images, 334 measurements of the irregular altered zone thicknesses were
273 calculated using GIMP image processing software. The average of these measurements for the AVM10
274 glass is around 659 nm. The minimum thickness measured is 78 nm and the maximum thickness
275 measured is 1.9 μm . The same process could not be repeated for other samples due to technical
276 difficulties.

277 (ii) Precipitation of Mg-rich phyllosilicates and other secondary precipitates: Both glass surfaces
278 were covered by secondary precipitates. SEM images showed well-developed leafy precipitates on both
279 AVM6-180 and AVM6-557 (figure 2(a) and figure 1(b)). Needle shaped precipitates were present
280 sporadically on the altered surface (figure 2(a)). In AVM6-557, these needle-shaped phases were much
281 more developed and formed clusters. As shown in figure 2(c) and 2(d), curiously, these clusters formed
282 in straight lines. It seems as though these phases preferentially formed along surface defects created
283 during sample preparation (polishing). TEM images also showed the presence of a layer of phyllosilicates
284 on the surface of the micro-sections that measured approx. 70 nm in AVM6-180 (Figure 2(b)) and
285 approx. 200-250 nm in AVM6-557 (figure 1 (b)). TEM-EDX analysis and EDS mapping of an altered zone
286 also indicated that the phyllosilicates were enriched in Mg, Fe and Na in addition to Si and they were
287 depleted in Al with respect to the pristine glass composition (supplementary data –section 3, figure S 6
288 and S 7). Figure S4 in supplementary data shows the enrichment of Mg in the phyllosilicate layer.

289 The leafy precipitates in AVM10-180 seemed to be under-developed and visually different in
290 comparison to AVM6. In AVM10-557, they were better developed than AVM10-180, as can be seen in
291 figure 2(f) in comparison to 2(e). This can also be affirmed by the SEM & TEM images provided in the
292 supplementary data-section 2, figure S 3. The quantity of the needle shaped crystalline phases also seem
293 lower than that on the AVM6 samples and the AVM10-557 samples seem to contain more of them than

294 AVM10-180 samples (supplementary data- figure S 2). The TEM images show a phyllosilicate layer of
295 approx. 300 nm thickness for AVM10-180 and approximately 70 nm thick phyllosilicate layer for AVM10-
296 557 (figures 2(e) and 2(f)). It is to be noted here that it is not the overall layer thickness, but just the
297 thickness of the phyllosilicate section.

298 (iii) The third similarity between AVM6 and AVM10 samples is the presence of a dense
299 homogeneous gel layer beneath the phyllosilicate layer but above the porous irregularly altered zones.
300 This gel layer is approximately 50 nm thick in AVM6-180 (figure 2(b)) and 70 nm thick in AVM6-557
301 (figure 1(b)). It is approx. 30 nm thick in AVM10-180 and AVM10-557 (figures 2(e) and 2(f) respectively).
302 This layer is enriched in Mg, Si and Ca, and sometimes slightly depleted in Al (supplementary data-
303 figures S 5, S 6, S 7 and S 9).

304 To summarize, under the tested conditions, AVM6 and AVM10 glasses alter similarly, which is
305 not the case for aqueous alteration of these glasses at the same temperature. The altered surface is
306 composed of a phyllosilicate layer at the top (few tens to a few hundreds of nm thick) that is composed
307 of Si, Al, Mg, Fe, Ca and Na. Underneath the phyllosilicates, TEM images have revealed a uniform gel
308 layer of a few tens of nm thickness that seems enriched in Mg and Si and depleted in Al, with respect to
309 the pristine glass. Porous irregularly altered zones are present in a heterogeneous/discontinuous manner
310 beneath the gel layer.

311

312 ***Identification of secondary precipitates***

313 The compositions of the phyllosilicates were analyzed using STEM-EDX. It is to be noted that the
314 Na concentration was not constant throughout the analysis. The Na atoms migrated under the beam
315 towards the resin. It was verified that the concentration of other major elements were not affected due
316 to long exposure to electron beam. The stoichiometry of elements (excluding Na) in the phyllosilicate
317 layer, calculated from the STEM-EDX analysis, for the four samples described in section 3.1.1 are
318 provided in table 2 (the estimated uncertainty is around 12% relative error). It can be noted that the
319 composition of phyllosilicates is variable during the alteration of different glasses. No correlation could
320 be identified with pristine glass compositions (Si/Al ratio for example) as was previously suggested [65].
321 The phyllosilicates formed on AVM6-180 and AVM6-557 have a very similar composition. The
322 stoichiometric ratio of Si/Mg suggests that the composition of the phyllosilicates formed on AVM6 glass
323 is similar to that of a di-octahedral smectite such as montmorillonite- $((\text{Na,Ca})_{0.33}(\text{Al,Fe,Mg})_2(\text{Si}_4\text{O}_{10})(\text{OH})_2 \cdot$

324 nH₂O), with slight variations in the composition based on the different transition metal substitutes
 325 available. The quantity of Al and other elements capable of occupying octahedral sites in the smectite
 326 (Mg, Fe) is not sufficient to envisage a tri-octahedral smectite.

327 The XRD patterns of the AVM6 samples showed an intense peak corresponding to (001)
 328 reflection at 15 Å (supplementary data figure S 10), which can be associated with montmorillonites [66].
 329 Other peaks, if present, were not clearly distinguishable from the background noise. Apart from the
 330 composition given by EDX analyses, the other method to distinguish di-octahedral smectites from tri-
 331 octahedral smectites is the appearance of the (060) reflection between 1.49 and 1.51 Å [67, 68]. It is
 332 difficult to distinguish the peaks around 1.51Å in the XRD patterns from the background noise. The
 333 physical magnitude represented by the (001) and (060) lines have different orientations. Therefore, it is
 334 possible that the intensity of one of the two peaks increases preferentially than the other. Nevertheless,
 335 these results confirm the formation of a di-octahedral smectite (montmorillonite) on the glass surface
 336 during vapor phase hydration in this study.

337 The composition of the phyllosilicates formed on AVM10-180 and AVM10-557 seem to differ, notably in
 338 Mg and O content. AVM10-180 sample has higher Mg and O contents. It is reasonable to suggest that
 339 the excess Mg and O in the AVM10-180 sample may be due to the presence of brucite (Mg(OH)₂), which
 340 is a well-known precursor of Mg-rich smectites [69-71]. No peaks were distinguishable in the XRD
 341 pattern, although the TEM images (figure 2(f) and supplementary data-figure S 3) clearly show the
 342 presence of a sheet-type mineral. The stoichiometric ratios suggest the possibility of either a di-
 343 octahedral smectite or a tri-octahedral smectite, depending on the incorporation of Al in tetrahedral
 344 sites or octahedral sites, respectively.

345 At this stage the exact composition of the smectite formed on AVM10 samples in this study cannot be
 346 affirmed with the available information. However, a possible smectite composition is proposed based on
 347 the EDX analyses of AVM10-557 (table 2) and the generic formula for tri-octahedral smectites proposed
 348 by Joly et al. [72]. This generic formula shown in equation 3.1.1.1 was earlier used by Arena et al. for
 349 identification of a phyllosilicate formed on nuclear waste glass simulant ISG in the presence of Fe and Mg
 350 (aqueous alteration, SA/V 20000 m⁻¹, 50°C, 511 days) [49]. "X" in equation 3.1.1.1 corresponds to cations
 351 other than Al that may occupy octahedral sites, such as Mg or Fe. The proposed composition is
 352 $[(\text{Si}_{3.85}\text{Al}_{0.15})((\text{Mg}, \text{Fe})_{2.13}\text{Al}_{0.87})\text{O}_{10}(\text{OH})_2]^{0.72+}[\text{Na}_{0.1}\text{Ca}_{0.1}]^{0.3+}$.

353 $[\text{Si}_{(4-a)}\text{Al}_a](\text{X}_{(3-b)}\text{Al}_b)\text{O}_{10}(\text{OH})_2]^{(a+b)-}[\text{X}_c\text{Na}_d\text{Ca}_e]^{(2c+d+2e)+}$ (Equation 3.1.1.1)

354 **3.1.2 AVMV4 and QMg**

355 The Si/Al ratio of the glass QMg is the same as the glass AVMV4. The SEM images of both the Mg-
356 containing glasses showed some similarities (i) The altered surface showed the presence of thread-like
357 carpet of precipitates along with μm sized cluster of fibrous precipitates in the SEM images of samples
358 altered for 180 days (AVMV4-180 and QMg-180) (figure 3(c) and 3(a) respectively). The altered surface of
359 the samples altered for 557 days (AVMV4-557 and QMg-557) showed the presence of holes of 400-500
360 nm in diameter and a gnawed appearance, with pit size of a few hundred nm, respectively (figure 3(d)
361 and 3(b) respectively) (ii) The altered layers of all four samples were not visible in SEM, indicating that
362 their thickness must be less than 100 nm. Irregularly altered zones were also not observed in the SEM
363 images.

364 TEM images of cross-section of AVMV4-557 show the presence of a gel layer of approximately 80 nm
365 thickness (figure 3(e) & (f) and Supplementary data, figure S11). Above this apparently homogeneous gel
366 layer, a mixture of amorphous and crystalline phases is distributed across the 5 μm cross-section in
367 varying thicknesses (200 nm to 20 nm). STEM image of QMg-180 showed an altered layer next to the
368 pristine glass that appears homogeneous and is between 40-60 nm in thickness (figure 4(a)). On the
369 surface of the altered layer, a layer of fibrous precipitates of 30-40 nm in thickness is present. The
370 electron diffraction patterns obtained from TEM imaging did not show any fringes in the zone of
371 precipitates, indicating that the precipitates are probably amorphous. The STEM-EDX analysis indicated
372 that the amorphous precipitates and the gel layer in the surface are enriched in Mg and Na and depleted
373 in Al, with respect to pristine glass (supplementary data-figure S 12).

374 **3.1.3 Q**

375 SEM images of Q altered for 180 days and 557 days (Q-180 & Q-557) do not show any recognizable
376 secondary precipitates. TEM image of a micro-section of Q-180 shows the presence of a seemingly
377 homogeneous altered layer of approx. 40 nm thickness (figure 4(b)). The pores that are visible on the
378 altered layer-pristine glass interface were formed / enlarged during exposure of the sample to the
379 electron beam.

380 **3.1.4 QCa**

381 SEM images of QCa altered for 180 days (QCa-180) show a few unidentified scattered precipitates on
382 the surface. TEM image of QCa-180 shows the presence of an apparently homogeneous altered layer of
383 approximately 80 nm (figure 5(a)). The difference in density between the pristine glass and gel layer
384 seems to be higher than other glasses observed.

385 Figure 5(b) shows the SEM image of QCa altered for 557 days (QCa-557). The sample surface contained
386 significantly more surface precipitates than QCa-180. There seems to be two types of secondary phases;
387 clusters of pointed needle-like secondary phases and cuboid precipitates. Figure 5(c) shows the SEM
388 image of sample cross-section. An altered layer of approx. 110-150 nm thickness is distinguishable due to
389 the contrast difference between the layer and the pristine glass. Calcite was identified by XRD patterns
390 on QCa-180 and QCa-557.

391 **3.2 Behavior of elements in the altered layers (ToF-SIMS profiles)**

392 Among all the characterization techniques presented in this study, ToF-SIMS and FTIR analyze the largest
393 surface area of the sample in a uniform manner for all six samples. Therefore, it is considered to be the
394 most suitable method for inter-comparison and the most representative in terms of element behavior in
395 the altered layer and the average depth of altered zone. Table 3 summarizes and compares the
396 thicknesses of the altered layers measured using ToF-SIMS and TEM images. The uncertainties of the
397 given values could not be calculated. The percent error associated with ToF-SIMS measures is generally
398 considered to be less than 3% [73]. Other factors contributing to the uncertainty are surface irregularity
399 due to precipitates, constant speed of abrasion used for the entire zone of analysis and
400 irregular/discontinuous altered zones. However, based on the coherence between the results of ToF-
401 SIMS and other characterization techniques, it can be presumed that the uncertainty associated with the
402 altered layer thicknesses can be overlooked.

403 Figure 6 presents the normalized ToF-SIMS profiles of the major elements present in the six glasses
404 altered for 180 days. The normalized ToF-SIMS profiles of all the elements present in all six samples
405 altered for 180 days and 557 days are presented in supplementary data (figures S 13 to S 19).

406 As observed in section 3.1, a similarity in the behavior of elements of the glasses AVM6 / AVM10 and
407 AVMV4 / QMg is noticeable. The striking similarity in the behavior of H, B, Al, Na and Mg in the glasses
408 AVMV4 and QMg are presented in supplementary data (figure S 20). Globally, for each glass, the
409 behavior of elements in the altered layer is remarkably similar among the two different samples altered
410 for two different durations. The four Mg-containing glasses show the presence of a layer of precipitates
411 towards the surface of the altered layer. As in SEM images, the thickness of this precipitate layer is much
412 higher in AVM6 (250-300 nm) and AVM10 (150-250 nm) than the AVMV4 and QMg glasses (<10 nm).
413 This precipitate layer mainly contains Mg, Na, Li, Cs and Fe (in addition to Si).

414 The altered layer-pristine glass interface is rather sharp for the samples AVMV4, Q, QCa and QMg, unlike
415 for the AVM6 and AVM10 samples. This apparently broad interface is due to the irregular and
416 discontinuous altered zones observed in SEM images. Therefore the thickness estimated for these two
417 glasses is considered as an average thickness of the analyzed zone. Based on the ToF-SIMS thickness
418 (boron) from table 3, the glasses AVM6 and AVM10 alter 10-30 times faster than the other four glasses.
419 Among the samples altered for 180 days, AVMV4, QCa and QMg alter 1.7 times faster than the glass Q.
420 Among the samples altered for 557 days, QCa alters almost twice that of AVMV4, QMg and Q. In testing
421 two samples of each glass for durations of 180 and 557 days, we considered that the rate of alteration
422 would be similar. However, the increase in the thickness of altered layer from 180 days to 557 days
423 suggests that the vapor hydration rate has decreased by a factor of 9.1 for AVMV4, 8.5 for QMg, 1.9 for
424 Q and 1.6 for QCa after 180 days of alteration (considering that the vapor hydration rate is constant
425 between 0-180 days and between 180-557 days).

426 In coherence with the STEM-EDX results, Al is depleted in the zone of surface precipitates of the Mg-
427 containing glasses, indicating that the Si/Al ratio is higher in the phyllosilicate layer than the glass.

428 The ToF-SIMS profiles, which have been normalized to Si and to PG, might give an impression
429 that many elements are depleted from the gel layer, even though not as extensively as boron. It seems
430 likely that this depletion is due to a migration of the element towards the surface to form precipitates. In
431 the zone of precipitates, the normalization with respect to Si creates an artificial depletion of elements
432 such as Zr, rare-earths and Al, because they are almost absent in the precipitate layer, towards the
433 surface. The elements which are really depleted (absent in gel layer and precipitate layer) are boron, Ca
434 in QCa and Na from the surface of Q. The retention of Ca is < 3% in the gel layer of QCa (in both QCa-180
435 and QCa-557).

436 **3.3 Porosity of the altered layer (SAXS)**

437 The porosity, pore-size and specific surface area values reported in this paper were calculated by
438 considering that the pores of the gel layer are filled with water. This assumption will be discussed later in
439 section 4. The data treatment was based on previous works [62-64] and is explained in detail in the
440 supplementary data (section1). q is the scattering vector in nm^{-1} and I_{corr} (cm^{-1}), calculated from
441 equation S9 in supplementary data, separates the scattering intensity in the high q domain by the pores
442 in the gel layer from the scattering in the low q domain by the grain envelopes.

443 AVM6 and AVM10: The plots of I_{corr} vs. q of these two glasses show a porod regime
444 ($I_{corr} \propto q^{-4}$). The SAXS spectra of these glasses are provided in figure S 21 (supplementary data). In both
445 glasses, the high q porod regime shifts to higher q values with time. However, porod's law cannot be
446 used to calculate the porosity and specific surface area of pores for these two glasses, since the SEM
447 images of the monolith samples indicate that these glass surfaces are covered with phyllosilicates.
448 Therefore, the SAXS diagram contains information regarding both the porosity of the gel layer and the
449 inter-layer spacing of the phyllosilicates and they cannot be deconvoluted.

450 AVM6 glass powders of particle size 2-5 μm that were prepared as described in section 2.1 were altered
451 at 50°C and 95% RH for 11 days, 31 days and 90 days, for the purpose of characterization by SAXS and
452 identification of possible trends in the evolution of the gel layer. These samples are referred to as AVM6-
453 11, AVM6-31 and AVM6-90. The I_{corr} vs. q plots of these glasses are shown in figure S 22
454 (supplementary data). Porod's law is respected at higher q values for all three samples including the
455 sample altered for only 11 days. The quantity of secondary phases on these samples altered for a short
456 duration is negligible (TEM images (not shown here) of AVM6 samples altered for 90 days at 50°C and
457 95% RH show that the surface precipitates are visually much less denser than the AVM6-180 samples).
458 Therefore, the porosity, pore-size and specific surface area of the gel layer can be calculated. The
459 porosity, pore diameter and specific surface area of AVM6-11 are 66%, 4.4 nm and 328 m^2/g
460 respectively; that of AVM6-31 are 47%, 4.5 nm and 235 m^2/g respectively; and that of AVM6-90 are 11%,
461 4.8 nm and 58.2 m^2/g . These values are recapitulated in table 4. It can be noticed that porosity decreases
462 with time, while pore size increases. The I_{corr} vs. q plot of AVM6-11 is distinctly different than that of
463 the other AVM6 samples. The shoulder corresponding to the highest intensity is at a higher q for the
464 AVM6-11 sample. This translates to a smaller average pore size than the other glasses [74]. However, the
465 porod regimes of the AVM6 samples altered for larger duration is shifted towards much higher q . This
466 suggests the presence of smaller pores in the samples that were altered for a duration longer than 11
467 days, even though the average pore-size increases with increase in duration of alteration.

468 AVMV4 and QMg: I_{corr} vs. q plot of these two glasses are similar in the sense that, neither of them
469 displays a porod's regime. The plots are shown in figure S 22 (supplementary data). The exponent D
470 ($I(Corr) \propto q^{-D}$) decreases with increase in duration of alteration, suggesting an increase in the
471 roughness of the pore-interface. It can be considered that the reason for the absence of a porod's
472 regime in the SAXS diagram is the interference of poorly crystallized precipitates. This means that the D
473 value, which varies between 3.4 to 2.6, is not representative of a rough pore-interface in the gel layer,

474 but rather a distortion of signal due to the presence of almost equal proportions of gel layer and poorly
475 crystalline precipitates.

476 Q and QCa: The I_{corr} vs. q plot of these two glasses exhibit a porod's regime (figure 7). The absence of a
477 substantial amount of secondary precipitates on the SEM and TEM images of the monolith samples
478 validate the use of these measurements to calculate the porosity, pore size and specific surface area of
479 pores. The porosity of Q-180 is 65% and decreases to 44% in the Q-557 sample. The pore diameter
480 increases from 4.3 nm in the Q-180 sample to 5 nm in the Q-557 nm. The surface area of pores also
481 decrease from 451 m²/g in the Q-180 sample to 264 m²/g in the Q-557 sample. The porosity of QCa-180
482 is 27%, which decreases to 9% in the QCa-557 sample. The pore diameter increases from 5.1 nm in QCa-
483 180 to 7.5 nm in QCa-557. The surface area of pores decrease from 158 m²/g in QCa-180 to 37.6 m²/g in
484 QCa-557. These calculated values are presented in table 4. Contrary to AVM6 and AVM10 samples
485 altered for 180 days and 557 days each, the high q porod's regime shift towards lower q at longer
486 duration of alteration. This indicates an increase in the average pore size with time. The higher pore sizes
487 of the QCa sample than the Q sample and the factor of increase in pore-size with time correspond well
488 with the magnitude of the shift in high- q porod's regime to lower q values for these samples as shown in
489 figure 7.

490 3.4 Hydration kinetics

491 3.4.1 FTIR spectroscopy

492 The hydration kinetics is followed by studying the evolution of the increase in the absorbance of the
493 band attributed to the OH stretching mode in SiOH molecules. For this, the absorbance around 3600 cm⁻¹
494 (OH stretching) measured at a given time of alteration (A) is reduced by the absorbance for the pristine
495 glass (A₀). Figure 8 shows the increase of (A-A₀) over time for all the six glasses until 557 days of
496 alteration. Figure 8(a) shows the difference in the increase of (A-A₀) versus time according to the glass
497 stoichiometry. The increase in absorbance of AVM6 glass is approximately twice that of AVM10, 10 times
498 that of QCa and 15 times that of AVMV4, Q and QMg. By correlating the increase in the absorbance of
499 the SiOH band to the thickness of altered layer formed and the vapor hydration rate, it seems that there
500 is an inflexion in the vapor hydration rate of all six glasses around approximately 6 months in the given
501 conditions. For the AVM10 glass, it seems that this inflexion occurs at 4 months. In figure 8(d), it seems
502 that there is acceleration in the vapor hydration rate between 60 and 120 days of alteration, followed by
503 a strong slowdown of the vapor hydration rate. Figures 8(c) shows the strikingly similar behavior of the
504 AVMV4 and QMg glasses. The inflexion seems to occur around 120 days of alteration. There also seems

505 to be a decrease in the absorbance after approximately 380 days of alteration. Figure 8(b) shows the
506 evolution of $(A-A_0)$ vs. time of the glasses Q and QCa. The inflexion seems to occur approximately around
507 180 days for the samples Q, QCa and AVM6. The factor by which the rate of increase of $(A-A_0)$ drops after
508 six months vary from 7.5 (AVM6) to 15 (AVM10).

509 **3.4.2 Alteration kinetics based on the different measurements of thickness**

510 The measurements of the thickness of the altered layers formed by ToF-SIMS and SEM/TEM images after
511 180 days and 557 days of vapor hydration of the six glasses are presented in table 3. It can be noticed
512 that the thickness measured by ToF-SIMS is lower than the thickness measured by SEM/TEM images for
513 four of the six glasses (AVMV4, Q, QCa and QMg). This is likely due to the fact that in ToF-SIMS, the layer
514 of precipitates and the gel layer might get abraded faster than the pristine sample due to the difference
515 in composition and their lower density. But the same speed of abrasion was used whatever the layer
516 considered. As a result, the thicknesses of the altered layers, which are a combination of the gel layers
517 and precipitate layers, are underestimated. Nevertheless, the thicknesses measured by ToF-SIMS and
518 TEM images are in the same order of magnitude. A second similarity between the thicknesses measured
519 by both techniques is that the sample Q has the smallest thickness among the four samples altered for
520 180 days and the thickness of the samples Q, QMg and AVMV4 are similar among the samples altered for
521 557 days. Therefore, it can be stated that the two techniques corroborate each other. In the case of the
522 glasses AVM6 and AVM10, which have an irregular alteration, ToF-SIMS provides an average altered
523 layer thickness in a relatively larger zone ($50 \times 50 \mu\text{m}^2$) and the SEM/TEM images have shown that the
524 thickness could vary from a few tens of nm to a few μm . The average thickness provided by ToF-SIMS is
525 useful to identify the relative durability of glasses. In addition, according to the FTIR results, the glasses
526 AVM6 and AVM10 alter 10-20 times faster than the other four glasses. This result is very well
527 corroborated by the ToF-SIMS results. While studying the alteration kinetics based on ToF-SIMS and
528 SEM/TEM images, the rate of formation of altered layer (in nm/day) after 180 days and 557 days
529 calculated by assuming linear alteration kinetics shows that the rate has decreased between 180 days
530 and 557 days of vapor hydration. This result is also explained very well by the FTIR spectroscopy, which
531 shows an inflexion in the rate of increase in $(A-A_0)$ with time after about 120-200 days of alteration. Thus
532 the alteration kinetics measured by three different techniques are coherent.

533 4. Discussion

534 **4.1 Morphology of the altered layer**

535 Figure 9 shows a schematic description of the different morphologies of the altered layer for all
536 six glasses altered under the same conditions. All six glasses present a homogeneous gel layer of tens of
537 nm thickness adjacent to the pristine glass. AVM6 and AVM10 present irregularly shaped, discontinuous
538 and more porous altered zones beneath the continuous gel layer. These two glasses contain significant
539 amount of well-developed Mg-rich smectites and needle-shaped precipitates (AVM6 has more of it than
540 AVM10). AVMV4 and QMg also present a layer of poorly-crystalline Mg-rich layer of precipitates on the
541 surface above the gel layer. However, the SEM images have shown that they are present in a much lesser
542 quantity than in AVM6 and AVM10. SEM images have not revealed any irregularly altered zones in these
543 glasses. Q and QCa glasses also contain precipitates on the surface of the gel layer, but unlike in the Mg-
544 containing glasses, they do not cover the glass surface. They are rather present in the form of crystals,
545 which are either isolated or in clusters.

546 The morphology of AVM6 and AVM10 altered samples is rather surprising, particularly because
547 of the presence of porous irregular altered zones beneath the homogeneous gel layer. Irregular
548 alteration has been noticed in literature [75-78], especially in atmospheric alteration studies. The
549 formation of a heterogeneous altered layer and craters are often attributed to a localized chemical
550 attack due to surface defaults such as cracks/scratches/fissures or deposit of dust particles/matter from
551 exposure to atmosphere or formation of hygroscopic salts locally on the surface or preferential/irregular
552 water condensation [22, 79, 80]. The unexpected part was the presence of the uniform and continuous
553 gel layer in-between phyllosilicates and irregular more porous discontinuous altered zones. A similar
554 dense gel layer formed in-between phyllosilicates and irregular porous zones could not be found in
555 literature. The closest analogy found was the gel layer formed during the aqueous alteration of a Si-B-Na-
556 Ca-Zr glass. In the cited studies, a dense gel layer was present on the altered surface and above a porous
557 gel layer. This denser gel layer was associated with pore-closure with time and passivating effect of the
558 gel layer [81-83]. However, in literature, a denser gel layer close to the unaltered glass and a porous gel
559 layer towards the glass surface and beneath secondary phases have been noticed [84]. Two possibilities
560 can be imagined in our study: (i) The hydration front is irregular; the pore closure due to reorganization
561 of the gel occurs at the surface in the region of the "oldest" gel, as suggested in the above mentioned
562 example [83]. (ii) The denser gel layer and the irregular, more porous, discontinuous altered zones were

563 formed or driven by two different mechanisms. The second assumption seems more likely and is
564 discussed further in section 4.5.

565 **4.2 Behaviour of elements (alkalis, Ca and B) in the altered zone**

566
567 Boron is depleted in the gel layer of all six glasses (less than 20% retention). Although it is useful
568 to estimate the altered layer thicknesses from ToF-SIMS profiles, its depletion is puzzling. It would be
569 logical to expect that elements are not lost from the altered layer during vapor phase hydration. The
570 depletion could mean that there is water condensation on glass surface followed by run-off. If this is the
571 case, the loss of other soluble elements such as Na and Li can be expected as well. However, Na is
572 retained to a higher extent than boron as can be seen in figure 6. The profiles of B, Na and Li do not
573 resemble each other. Therefore, the possibility of evaporation of boric acid species at 50°C and 95% RH
574 should also be investigated [85, 86].

575 Hence, a vapor hydration experiment was conducted with 0.6 g of borosilicate glass (QMg)
576 powder of particle size 20-40 μm (90°C, 98% RH, 153 days) using the protocol previously used on glass
577 monoliths by Neeway et al. [28]. The glass powder was placed in a cup inside the reactor above NaCl
578 solution that was used to impose relative humidity. The set-up was arranged in such a way that the
579 water that condenses on glass powders in the cup cannot run-off. Despite the set-up, 0.7 ± 0.1 mg of
580 boron was present in the NaCl solution at the end of the experiment. The vapor hydration rate of QMg at
581 90°C was estimated based on unpublished results and using this value, it was estimated that $27\pm 6\%$ of
582 boron from the altered layer was lost by evaporation. This experiment shows the possibility of
583 evaporation of boron/boric acid species and indicates that at 50°C, probably only a small fraction of
584 boron escapes due to volatility and a large fraction must be lost due to condensation and run-off.

585 Ca is depleted to a higher extent than boron in the QCa glass (<2% retention). It can be justified
586 by the formation of calcite crystals on the surface of the glass, which may adhere poorly. For a glass that
587 has only 52 nm thick altered layer, sufficient quantity of calcite had precipitated to be identified in XRD
588 pattern. The depletion of Na towards the surface of the Q glass could probably be due to formation of
589 carbonates (although undetected). In the other glasses, Na is well retained in the gel layer. In figure 6, a
590 certain similarity can be observed in the profile of Na and H for all glasses. This suggests that Na is
591 reactive and might be linked to inter-diffusion reaction. Despite being probably released from the glass
592 network, Na is still well retained in the gel layer (except in Q). It may be present in porewater, form

593 precipitates or may participate in the hydrolysis of $\equiv\text{Si-O-Si}\equiv$ bonds to form $\equiv\text{Si-O}^-\dots\text{Na}^+$ bonds, as
594 suggested in literature [39].

595 4.3 Porosity of the altered layer

596
597 During the SAXS data treatment, it was assumed that the pores in the gel layer are filled with water. This
598 assumption is supported by the calculation of the threshold pore-size by Kelvin's equation (equation
599 4.3.1) [87], below which, water is expected to condense in pores due to capillary effect. This threshold
600 pore-radius was calculated to be 9.2 nm at 50°C and 95% RH from equation 4.3.1. The maximum value of
601 the pore-radius measured through SAXS is <4 nm. Therefore, it seems highly probable that the pores are
602 filled with water. The porosity of the gels was also calculated by considering that the pores are filled with
603 air, but in this case, the calculated porosity values were unrealistic. This further reinforces our
604 assumption that the pores are filled with water. However, a certain uncertainty is associated with this
605 assumption. Even if it is considered that the pores are indeed filled with water during the experiment, it
606 is unclear if the water stays in the pores during characterization or it evaporates/escapes into the
607 atmosphere once the sample is removed from the humid and hot atmosphere (95% RH & 50°C). Data
608 analysis has been carried out despite this uncertainty by considering that water remains inside the pores,
609 since the samples were not exposed to high temperatures or desiccators during storage until
610 characterization. Specific studies to carefully assess the impact of this uncertainty on data treatment are
611 a necessary perspective.

$$612 \ln \frac{P}{P_0} = -\frac{2HyV_l}{RT} \quad (\text{Equation 4.3.1})$$

613 The values of the porosity, specific surface area of the pores and the pore-radiuses are in the same order
614 of magnitude as those observed in published aqueous alteration experiments of borosilicate glasses [63,
615 88, 89]. 66% porosity of the gel layer of Q-180 and AVM6-11 (table 4) seem relatively high, especially
616 while comparing with TEM images of Q-180, which do not show a very porous altered layer. This means
617 that either the porosity measured by SAXS is overestimated or there is some other unknown mechanism
618 that could explain such high porosity values, which needs further investigation of the gel layer formed on
619 these glasses. This porosity value may be overestimated due to the volume fraction of gel used in data
620 treatment, which is reasonably assumed based on altered layer thicknesses of the gel layer formed on
621 monoliths. This being said, such high porosity values have also been reported during aqueous alteration
622 of glasses [63, 89].

623 From table 4, all three glasses show a decrease in porosity and surface area of pores with time and an
624 increase in the average pore size with time. This evolution in our vapor hydration study is similar to the
625 results of an aqueous alteration study conducted by Girard et al., who altered glasses containing Si, B,
626 Na, Ca and Zr in aqueous medium at an SA/V (surface area of glass/solution volume) ratio of 3000 m^{-1} at
627 90°C for time periods up to 96 h [89]. According to their results, the porosity, depending on composition,
628 increased rapidly to a maximum value within a few hours of glass alteration. After reaching maxima, the
629 porosity and specific surface area of pores decreased with increasing time of alteration, probably due to
630 a shrinking gel and the pore-size increased due to either coalescence of pores or further dissolution at
631 the pore walls. The initially high porosity after a few hours of glass leaching was attributed to leaching of
632 Si from the solution without re-condensation until the solution becomes saturated with respect to Si.
633 This theory was based on the calculation of an estimated porosity from leachate composition. In this
634 study, the leachate cannot be sampled since it is a vapor phase alteration. Therefore, an acceptable
635 estimated porosity cannot be calculated using the leached fraction of soluble elements such as B and Na,
636 as was done in literature [89]. However, an estimated porosity was calculated based on the retention
637 factor R of elements in the gel layer calculated from ToF-SIMS profiles of monoliths and the volume
638 fraction occupied by oxides ϕ_i as shown in section 8 of the supplementary data.

639 The estimated porosity values thus calculated vary between 14% and 25% (table S 1-supplementary
640 data). For all six glasses, the estimated porosity value at 557 days is less than the estimated porosity
641 value at 180 days. This decrease in this estimated porosity is coherent with the SAXS results.
642 Nevertheless, the values of porosity calculated by SAXS for the glass Q is 3.2 to 3.9 times higher than the
643 hypothetical values estimated by depleted elements (based on ToF-SIMS results). It can be supposed
644 that the porosity estimated by retention of elements in the gel layer calculated based on ToF-SIMS
645 analysis is probably underestimated, because it considers that the elements present in the porewater of
646 the gel layer are a part of the gel layer network. There is the possibility of overestimation of porosity
647 values by SAXS as well. In the cases in which the SAXS porosity is lower than the porosity estimated from
648 SIMS data, different hypotheses such as a shrinking gel or precipitation of colloids or secondary phases
649 (calcite) in the pores could be proposed based on literature [89, 90].

650 **4.4 Hydration Kinetics**

651 Overall, the relative durability of the glasses identified by the increase in absorbance of the SiOH
652 molecules in FTIR spectra are coherent with that measured by other characterization techniques. These
653 results reinforce the argument that FTIR spectroscopy is a good method to follow vapor hydration

654 kinetics, in the absence of sampling techniques to determine soluble element concentrations in the
655 leachate. All glasses showed an inflexion in the vapor hydration kinetics after 120 or 180 days of
656 alteration. The cause for this inflexion has not yet been investigated. But such inflexion has been
657 observed earlier in literature, notably in the experiments conducted on CSD-B (inactive simulant of
658 intermediate-level long lived waste glass) and SON68 glasses after about 100-200 days of alteration (at
659 35-90°C) [29, 58].

660 **4.5 Influence of glass composition and insights into vapor hydration mechanisms**

661
662 The difference in the vapor hydration kinetics of AVM6, AVM10 and AVMV4 is an indication of the
663 significant effect of glass composition on glass hydration. The effect of stoichiometry on the relative
664 durability of AVM glasses in aqueous medium was already investigated [46, 47]. According to these
665 studies, the three major parameters affecting glass durability in water under a given condition were pH,
666 Mg and Al concentration. When $\text{pH}_{50^\circ\text{C}} > 9$, alteration rates increase due to precipitation of Mg-
667 aluminosilicates. Moreover, AVM glasses contain very little Ca. Therefore, it is considered that the role of
668 charge compensating atoms of $[\text{AlO}_4]^-$ units is preferentially occupied by Mg (the preference in gels
669 decreases in the order $\text{Ca}^{2+} > \text{Mg}^{2+} > \text{Na}^+$). Thus, a higher quantity of Al in the gel layer probably retains
670 higher quantity of Mg in the gel, thereby, increasing the passivation properties of the gel layer [46, 47].
671 This interpretation was used to explain the highest relative durability of AVM10 glass in aqueous
672 medium, since it contains the highest Al concentration among the three glasses.

673 In our vapor hydration study, AVM10 glass is one of the two least durable glasses. Therefore, the glass
674 durability is not simply linearly dependent on Al concentration. The reason for this could be that the
675 AVM10 glass contains higher MgO molar concentration than Al_2O_3 (i.e. molar ratio of $\text{Al}_2\text{O}_3/\text{MgO} < 1$).
676 Therefore, as an extreme case, if it is considered that all the $[\text{AlO}_4]^-$ units in the gel layer are charge
677 compensated by Mg^{2+} ions, there is still an excess of Mg that can saturate the molecular water
678 layers/porewater to form Mg-silicates, thus driving the glass alteration. The difference in the relative
679 durability of AVM10 between aqueous medium and vapor phase could be due to the possibly higher pH
680 of the very small volume of water in vapor phase, thereby promoting the precipitation of Mg-silicates
681 during vapor hydration and not as much during aqueous alteration.

682 The lower durability of AVM6 glass in this vapor hydration study can also be explained using the same
683 interpretation (i.e. molar ratio of $\text{Al}_2\text{O}_3/\text{MgO} < 1$). The extensive alteration of AVM6 and AVM10, which is
684 manifested as irregularly altered zones, could be driven by the precipitation of a significant amount of
685 Mg-silicates. On the other hand, this ratio is equal to 1 for AVMV4 and is greater than 1 for QMg,

686 suggesting that, Mg could be principally occupying the role of charge compensating atom and therefore
687 be less available for participation in the formation of secondary phases. As a result, the vapor hydration
688 of these two glasses may not be accelerated due to the precipitation of Mg-silicates.

689
690 The lack of structural study to support this assumption definitely needs to be acknowledged. The
691 distribution of coordination number of Al in the gel layer was not studied. Incidentally, recent
692 publications have shown that due to the high cation field strength of Mg, the presence of this element in
693 the glass network increases the fraction of ^(v)Al and ^(vi)Al and ⁽ⁱⁱⁱ⁾B, and thus contributes to glass
694 depolymerisation [91, 92]. As a matter of fact, the fraction of ^(iv)B in the Mg containing glasses in our
695 study were lower than that in the glasses Q and QCa (section 2.1). It is also suggested that some of the
696 Mg could be acting as a network former [92]. Therefore, there is a need to better understand the role of
697 Mg in the glass as well as in the gel, its impact on the gel structure and especially the competition
698 between ions to compensate the charge of $[\text{AlO}_4]^-$ units.

699
700 In order to understand the specific effect of Ca and Mg on vapor hydration of glasses, the results of the
701 simplified glasses Q, QCa and QMg need to be focused upon. Table 3 shows that QCa and QMg alter 1.6
702 to 1.7 times faster than Q, among the samples altered for 180 days. This can be construed to be a
703 negative effect of Ca and Mg, due to the precipitation of calcite and Mg-rich precipitates. However, the
704 NBO fraction (table 1) indicates that these two glasses have higher fraction of NBOs than the glass Q.
705 From figure S 23 in supplementary data, it can be seen that, among the glasses altered for 180 days, the
706 higher the NBO fraction, the higher the thickness of the altered layer formed. This relation seems to be
707 linear for the glasses AVMV4, Q, QCa and QMg and a sharp rise is noted for the glasses AVM6 and
708 AVM10, which have undergone extensive alteration due to secondary phases precipitation. Therefore,
709 the slightly higher altered layer thicknesses of the glasses QCa and QMg in comparison to Q could be due
710 to the lower resistance to network hydrolysis and not a negative effect of Ca or Mg. This suggests that
711 network-hydrolysis could be the rate limiting mechanism of formation of the uniform gel layer.

712 Among the samples altered for 557 days, the altered layer thickness of QCa is twice that of Q and QMg.
713 This change in the relative durability of glasses with a longer duration can be explained by considering
714 the presence of a passivating altered layer. The SAXS results also hint at a reorganization of the
715 homogeneous gel layer, at least in the case of Q, QCa and AVM6. The inflexion in the vapor hydration
716 kinetics (FTIR spectroscopy) after 180 days approximately strongly suggests the presence of a passivation

717 mechanism of the gel layer in all six glasses. After six months, the altered layer of QMg (and AVMV4)
718 could have become more passivating than that of Q and QCa. This presumption is based on ToF-SIMS
719 profiles, which show that the retention of Ca in the gel layer is less than 1% and Na is less retained in the
720 gel layer of Q. The gel layer of QMg (and AVMV4) retains a higher quantity of Mg. It has already been
721 shown that the retention of Mg increases the passivation properties of the gel layer [46]. This implies
722 that the rate-limiting vapor hydration mechanism changes, probably to diffusion of species through the
723 gel layer, after the inflexion of vapor hydration rate due to the formation of a passivating altered layer.
724 This is in agreement with the structure discussion above for AVMV4 and QMg.

725 In brief, the specific effect of Ca or Mg could not be seen in this vapor hydration study because the
726 excessive concentration of Al (molar ratio of $\text{Al}_2\text{O}_3/(\text{MgO} \text{ or } \text{CaO}) \geq 1$) has masked the possible negative
727 effect that Ca or Mg could have due to secondary phase precipitation. The presence of Al in the glass
728 increases its resistance to network hydrolysis since $\equiv\text{Si-O-Al}\equiv$ bonds require more energy to be broken
729 than $\equiv\text{Si-O-B-}$ or $\equiv\text{Si-O-Si}\equiv$ bonds [54, 93].

730 The interpretation of the results suggests that the rate-limiting mechanism of formation of the gel layer
731 in vapor hydration is network hydrolysis in this study. This conclusion is reinforced by the fact that
732 AVM10, which has the highest Al content in the pristine glass, has the lowest thickness of the
733 homogeneous gel layer (15-30 nm in TEM), even if the overall alteration layers cumulate to larger
734 thickness after secondary phases form.

735 The formation of irregularly shaped (few tens of nm to few μm thick), discontinuous, more porous
736 altered zones behind the homogeneous gel layer in AVM6 and AVM10 glasses seem to be driven by
737 precipitation of significant quantities of Mg-silicates. During vapor hydration, extensive alteration due to
738 secondary phase precipitation is naturally local (and hence irregular). Thus, it is possible that in AVM6
739 and AVM10, the two types of altered zones were formed by two parallel mechanisms.

740 The precipitated secondary phases found at the surface in the other four glasses (AVMV4, Q, QCa and
741 QMg) are probably a consequence of the release of alkaline-earth elements from glass network and do
742 not drive the formation of their homogeneous gel layer.

743 **4.6 Vapor hydration vs. aqueous alteration**

744 Glass AVM6 was found to be the glass of lowest durability of the series in aqueous leaching and in the
745 present vapor phase alterations. However, a reversal of glass durability in vapor phase and aqueous
746 medium has been observed between the glasses AVM10 and AVMV4. The residual alteration rates of the
747 three complex glasses in aqueous medium (initially pure water, 50°C, $\text{SA}/\text{V}=5500 \text{ m}^{-1}$, values measured
748 between 5-10 years of alteration) are: AVM6- $5.1 \times 10^{-4} \text{ g}/\text{m}^2/\text{day}$; AVM10- $9 \times 10^{-5} \text{ g}/\text{m}^2/\text{day}$; [46]; AVMV4-

749 5.6×10^{-4} g/m²/day (personal communication-value estimated based on a statistic interpolation model).
750 The difference may be due to changes in the solution chemistry of the very low volume of water
751 available for glass dissolution in vapor phase. This small volume of water may get rapidly saturated with
752 respect to secondary phases that are clearly different than those that precipitate during aqueous
753 alteration.

754 The smectites formed during vapor hydration, as identified through STEM-EDX analyses (see sub-section
755 of 3.1.1), seem to be different than those that form during aqueous alteration of the same glasses. A tri-
756 octahedral smectite was identified on AVM6 altered in aqueous medium [46], while a di-octahedral
757 smectite (type montmorillonite) was identified during this vapor hydration study of AVM6. The
758 phyllosilicate formed in vapor phase contained 75% lower Al, 40% lower Mg and 10 times higher Fe
759 content.

760 The phyllosilicate composition obtained on AVM10 in this study was compared with the phyllosilicate
761 composition obtained during the aqueous alteration of AVM10 in the study conducted by Thien et al.
762 (SA/V 5500 m⁻¹, 50°C, 2500 days, initially pure water and 400 mg/L of MgCl₂·6H₂O added after 114 days)
763 [94]. The concentration of Al in the phyllosilicate of our study was 25% lower than the Al concentration
764 in the smectite identified by Thien et al [94]. Similarly, the concentration of Mg was 30% lower and the
765 concentration of Fe was three times higher.

766 This shows that caution needs to be taken while extrapolating aqueous alteration results to
767 vapor hydration by considering that vapor hydration is equivalent to aqueous alteration at a very high
768 SA/V ratio. Certain studies conducted vapor hydration tests in extreme conditions (150-200°C, 100% RH)
769 to predict the secondary phases that would form during long-term aqueous alteration of glasses [36].
770 Here, it is clearly shown that the same phases do not precipitate in both media.

771 One similarity between aqueous alteration and vapor hydration studies of glasses is the texture
772 of the gel layer. SAXS data indicated that the porosity, pore-size and specific surface area values are in
773 the same order of magnitude and evolve similarly with time in the two glasses of different compositions
774 and in different alteration conditions [88, 95]. This could imply a similar mechanism of formation of the
775 gel layer.

776 5. Conclusion

777 In order to study the influence of glass composition on vapor hydration kinetics, three complex glasses
778 (>20 oxides) and three simplified glasses (4 or 5 oxides) were altered in vapor phase (at 50°C and 95%

779 RH) for a period of 180 days and 557 days. Based on the analysis of the characterization results of the
780 altered samples, it seems that network hydrolysis is the rate limiting mechanism of formation of the gel
781 layer during vapor hydration of these glasses. Under conditions that are favorable for the precipitation of
782 secondary phases, it seems that the vapor hydration kinetics is accelerated in a localized manner, leading
783 to the formation of irregularly shaped, discontinuous altered zones that could be up to a few μm thick.
784 The presence of alkaline-earth elements (such as Mg or Ca) seems to make the glass more reactive, since
785 they actively participate in the formation of secondary phases. However, the negative effect of these
786 elements is attenuated by the presence of Al, since Al increases the resistance to hydrolysis of glass
787 network and its presence in the gel layer retains alkaline-earth elements to compensate $[\text{AlO}_4]^-$ entities.
788 Therefore, when the molar ratio of $\text{Al}_2\text{O}_3/(\text{MgO or CaO}) \geq 1$, the positive effect of Al prevails over the
789 expected negative effect of Ca or Mg and therefore the glass is relatively more durable. When the ratio is
790 < 1 , the negative effect of Ca or Mg prevails. For this reason no specific effect of Ca or Mg on vapor
791 hydration of the three simplified glasses could be seen (molar ratio of $\text{Al}_2\text{O}_3/(\text{MgO or CaO}) \geq 1$).

792 Apart from this principal result, two types of altered layer morphologies have been identified. The
793 porous texture of the gel layer of a vapor hydrated glass has been investigated using SAXS. The measured
794 pore-diameters vary between 4.3-7.5 nm, similar to the pore-sizes found in the gel layer formed on
795 various similar glasses during aqueous alteration.

796 It has been shown that the vapor hydration mechanism changes with glass composition and time. The
797 rate of vapor hydration evaluated in FTIR showed a decrease between 180 days and 300 days, which
798 validate the formation of a passivating layer.

799 Based on this study, a few perspectives have been identified. The structural role of Mg in the glass and
800 gel and its capability to compensate negative charge of $[\text{AlO}_4]^-$ units needs to be investigated to
801 understand the positive effect of Al that prevails over the negative effect of Mg on glass durability.
802 Aqueous alteration of the same glasses at very basic pH ($\text{pH}_{50^\circ\text{C}} > 11$) may provoke the precipitation of
803 similar secondary phases in order to observe the relative durability of these glasses. This might help to
804 affirm or refute the hypothesis of importance of molar ratio of $\text{Al}_2\text{O}_3/\text{MgO}$ on glass durability.

805 It would also be interesting to conduct vapor hydration experiments of the same glasses at a higher
806 temperature ($> 90^\circ\text{C}$) to study if possibly favorable conditions for secondary phase precipitation drives
807 vapor hydration or if the rate-controlling mechanism is network-hydrolysis as in low temperatures
808 (50°C). It is also necessary to investigate if the gel layers formed during vapor hydration have any

809 protective effect against aqueous alteration, since it is expected that a vapor hydrated nuclear waste
810 glass would eventually be altered in groundwater of the repository site.

811 Acknowledgements

812 We would like to thank Laurent Duffours (PrimeVerre) for preparation of the polished glass monoliths,
813 Géraldine Parisot (CEA) for ICP-OES analysis of glass powders, Jean-Pierre Mestre (CEA) and Marie Fenart
814 (CEA) for the SEM images, Myriam Chartier (CEA) for XRD patterns, Laurent Dupuy and Elodie Chauvet
815 (TESCAN Analytics) for the ToF-SIMS profiles and Jeremy Causse (ICSM) for SAXS data acquisition. This
816 study was supported by CEA and EDF (Electricité de France). We would like to particularly thank Florent
817 Tocino and Hélène Schneider (EDF) for their support. We also thank the two anonymous reviewers for
818 their helpful comments and constructive feedback.

819 Data Availability

820 The SEM and TEM data supporting the findings are available within the article and the supplementary
821 information. The processed data of SAXS, ToF-SIMS, NMR spectroscopy and XRD apparatuses are also
822 available within the article and supplementary information. The raw data of SAXS, ToF-SIMS, NMR
823 spectroscopy and XRD apparatuses required to reproduce these findings cannot be shared at this time
824 due to technical and time limitations. However, they can be shared by the corresponding author upon
825 reasonable request.

826 References

- 827 1. Friedman, I. and W.D. Long, *Volcanic glasses, their origins and alteration processes*. Journal of
828 Non-Crystalline Solids, 1984. **67**: p. 127-133.
- 829 2. Verney-Carron, A., S. Gin, and G. Libourel, *A fractured roman glass block altered for 1800 years in*
830 *seawater: Analogy with nuclear waste glass in a deep geological repository*. Geochimica et
831 Cosmochimica Acta, 2008. **72**(22): p. 5372-5385.
- 832 3. ANDRA-Collectif, *Dossier d'options de sûreté - Partie après fermeture (DOS-AF)*. 2016, ANDRA. p.
833 1-467.
- 834 4. Poinssot, C. and S. Gin, *Long-term Behavior Science: The cornerstone approach for reliably*
835 *assessing the long-term performance of nuclear waste*. Journal of Nuclear Materials, 2012.
836 **420**(1-3): p. 182-192.
- 837 5. De Echave, T., et al., *Influence of iron on the alteration of the SON68 nuclear glass in the Callovo-*
838 *Oxfordian groundwater*. Applied Geochemistry, 2019. **100**: p. 268-278.
- 839 6. De Echave, T., et al., *Effect of clayey groundwater on the dissolution rate of SON68 simulated*
840 *nuclear waste glass at 70 °C*. Journal of Nuclear Materials, 2018. **503**: p. 279-289.
- 841 7. Suzuki-Muresan, T., et al., *Alteration of vitrified intermediate level nuclear waste in alkaline*
842 *media: effects of cementitious materials, pH and temperature*. RSC Advances, 2018. **8**(66): p.
843 37665-37680.

- 844 8. Rieke, P.C., et al., *Adaptation of the GRAAL model of Glass Reactivity to accommodate non-linear*
845 *diffusivity*. Journal of Nuclear Materials, 2018. **512**: p. 79-93.
- 846 9. Frugier, P., et al., *Modeling glass corrosion with GRAAL*. npj Materials Degradation, 2018. **2**(1): p.
847 35.
- 848 10. Ducasse, T., et al., *Alteration of synthetic basaltic glass in silica saturated conditions: Analogy*
849 *with nuclear glass*. Applied Geochemistry, 2018. **97**: p. 19-31.
- 850 11. Gin, S., et al., *Atom-Probe Tomography, TEM and ToF-SIMS study of borosilicate glass alteration*
851 *rim: A multiscale approach to investigating rate-limiting mechanisms*. Geochimica et
852 Cosmochimica Acta, 2017. **202**: p. 57-76.
- 853 12. Collin, M., et al., *Structure of International Simple Glass and properties of passivating layer*
854 *formed in circumneutral pH conditions*. npj Materials Degradation, 2018. **2**(1): p. 4.
- 855 13. Grambow, B. and R. Muller, *First-order dissolution rate law and the role of surface layers in glass*
856 *performance assessment*. Journal of Nuclear Materials, 2001. **298**(1,2): p. 112-124.
- 857 14. Hellmann, R., et al., *Nanometre-scale evidence for interfacial dissolution-precipitation control*
858 *of silicate glass corrosion*. Nature Materials, 2015. **14**(3): p. 307-311.
- 859 15. Geisler, T., et al., *Aqueous corrosion of borosilicate glass under acidic conditions: A new corrosion*
860 *mechanism*. Journal of Non-Crystalline Solids, 2010. **356**(28-30): p. 1458-1465.
- 861 16. Ebert, W.L., R.F. Hoburg, and J.K. Bates, *The sorption of water on obsidian and nuclear waste*
862 *glass*. Phys. Chem. Glasses, 1991. **32**(4): p. 133-137.
- 863 17. Gong, W.L., et al., *Secondary phase formation and the microstructural evolution of surface layers*
864 *during vapor phase alteration of the French SON68 nuclear waste glass at 200°C*, in *Scientific*
865 *Basis for Nuclear Waste Management XIX*, W.M. Murphy and D.A. Knecht, Editors. 1996, Mater.
866 Res. Soc: Philadelphia, PA, USA. p. 197-204.
- 867 18. Bates, J.K., M.G. Seitz, and M.J. Steindler, *The relevance of vapor phase hydration aging to*
868 *nuclear waste isolation*. Nuclear and Chemical Waste Management, 1984. **5**: p. 63-73.
- 869 19. Bates, J.K., et al., *Issues affecting the prediction of glass reactivity in an unsaturated*
870 *environment*. Journal of Nuclear Materials, 1992. **190**: p. 198-227.
- 871 20. Bates, J.K., et al., *The hydration alteration of a commercial nuclear waste glass*. Chemical
872 Geology, 1985. **51**(1): p. 79-87.
- 873 21. Abrajano, T., J.K. Bates, and C.D. Byers, *Aqueous corrosion of natural and nuclear waste glasses I.*
874 *Comparative rates of hydration in liquid and vapor environments at elevated temperatures*.
875 Journal of Non Crystalline Solids, 1986. **84**: p. 251-257.
- 876 22. Abrajano, T.A., Jr., J.K. Bates, and J.J. Mazer, *Aqueous corrosion of natural and nuclear waste*
877 *glasses. II. Mechanisms of vapor hydration of nuclear waste glasses*. Journal of Non-Crystalline
878 Solids, 1989. **108**: p. 269-288.
- 879 23. Gong, W.L., et al., *Analytical electron microscopy study of surface layers formed on the French*
880 *SON68 nuclear waste glass during vapor hydration at 200°C*. Journal of Nuclear Materials, 1998.
881 **254**(2): p. 249-265.
- 882 24. Pierce, E.M., et al., *The Accelerated Weathering of a Radioactive Low-Activity Waste Glass Under*
883 *Hydraulically Unsaturated Conditions: Experimental Results from a Pressurized Unsaturated Flow*
884 *Test*. Nuclear Technology, 2006. **155**(2): p. 149-165.
- 885 25. McKeown, D.A., et al., *Tc and Re Behavior in Borosilicate Waste Glass Vapor Hydration Tests*.
886 Environmental Science & Technology, 2007. **41**(2): p. 431-436.
- 887 26. Buechele, A.C., et al., *Tc and Re behavior in borosilicate waste glass vapor hydration tests II*.
888 Journal of nuclear materials, 2012. **429**(1-3): p. 159-165.
- 889 27. Cassingham, N.J., et al., *Alteration layer formation of Ca- and Zn-oxide bearing alkali borosilicate*
890 *glasses for immobilisation of UK high level waste: A vapour hydration study*. Journal of Nuclear
891 Materials, 2016. **479**: p. 639-646.

- 892 28. Neeway, J., et al., *Vapor hydration of SON68 glass from 90 °C to 200 °C: A kinetic study and*
893 *corrosion products investigation*. Journal of Non Crystalline Solids, 2012. **358**(21): p. 2894-2905.
- 894 29. Chaou, A., et al., *Vapor hydration of a simulated borosilicate nuclear waste glass in unsaturated*
895 *conditions at 50 °C and 90 °C*. RSCC Advances, 2015. **5**(64538).
- 896 30. Chaou, A., et al., *The role of pH in the vapor hydration at 175 °C of the French SON68 glass*.
897 Applied Geochemistry, 2017. **76**: p. 22-35.
- 898 31. Bouakkaz, R., A. Abdelouas, and B. Grambow, *Kinetic study and structural evolution of SON68*
899 *nuclear waste glass altered from 35 to 125 °C under unsaturated H₂O and D₂O¹⁸ vapour*
900 *conditions*. Corrosion Science, 2018. **134**: p. 1-16.
- 901 32. Abdelouas, A., et al., *A Preliminary Investigation of the ISG Glass Vapor Hydration*.
902 INTERNATIONAL JOURNAL OF APPLIED GLASS SCIENCE, 2013. **4**(4): p. 307-316.
- 903 33. Chaou, A.A., et al., *The French SON68 glass vapor hydration under different atmospheres*.
904 Procedia Materials Science, 2014. **7** p. 179 – 185.
- 905 34. Collectif, *Référentiel du comportement des colis de déchets HA-MAVL - Tome 2 - Déchets vitrifiés*,
906 ANDRA and CEA, Editors. 2012. p. 1-548.
- 907 35. Ebert, W.L. and J.K. Bates, *The reaction of synthetic nuclear waste glass in steam and*
908 *hydrothermal solution*. 1990, United States: Materials Research Society.
- 909 36. Ebert, W.L., J.K. Bates, and W.L. Bourcier, *The hydration of borosilicate waste glass in liquid*
910 *water and steam at 200° C*. Waste Management, 1991. **11**: p. 205-221.
- 911 37. Moriya, Y. and M. Nogami, *Hydration of silicate glass in steam atmosphere*. Journal of Non-
912 Crystalline Solids, 1980. **38**: p. 667-672.
- 913 38. Wronkiewicz, D.J., J.E. Young, and J.K. Bates, *Effects of alpha and gamma radiation on glass*
914 *reaction in an unsaturated environment*, in *Scientific Basis for Nuclear Waste Management*.
915 1991, Mater. Res. Soc. p. 99-106.
- 916 39. Alloteau, F., et al., *New insight into atmospheric alteration of alkali-lime silicate glasses*.
917 Corrosion Science, 2017. **122**: p. 12-25.
- 918 40. Sessegolo, L., et al., *Long-term weathering rate of stained-glass windows using H and O isotopes*.
919 npj Materials Degradation, 2018. **2**(1): p. 17.
- 920 41. Gentaz, L., et al., *Role of secondary phases in the scaling of stained glass windows exposed to*
921 *rain*. Corrosion Science, 2016. **109**: p. 206-216.
- 922 42. Kudriavtsev, Y., et al., *Water vapor interaction with borosilicate glass*. Solid State Ionics, 2018.
923 **321**: p. 122-125.
- 924 43. Bunker, B.C., *Molecular mechanisms for corrosion of silica and silicate glasses*. Journal of Non-
925 Crystalline Solids, 1994. **179**: p. 300-308.
- 926 44. Kudriavtsev, Y., R. Asomoza-Palacio, and L. Manzanilla-Naim, *Interaction of water vapor with*
927 *silicate glass surfaces: Mass-spectrometric investigations*. Technical Physics Letters, 2017. **43**(5):
928 p. 447-449.
- 929 45. Cunnane, J.C., et al., *High-level nuclear-waste borosilicate glass : a compendium of*
930 *characteristics.*, in *Scientific Basis for Nuclear Waste Management XVI*, C.G. Interrante and R.T.
931 Pabalan, Editors. 1993, Mater. Res. Soc.: Pittsburgh, PA. p. 225-232.
- 932 46. Thien, B., et al., *The dual effect of Mg on the long-term alteration rate of AVM nuclear waste*
933 *glasses*. Journal of Nuclear Materials, 2012. **427**: p. 297-310.
- 934 47. Thien, B., *Développement des bases théoriques nécessaires à la modélisation de la vitesse*
935 *résiduelle d'altération en milieu aqueux des verres nucléaires AVM*. 2010, Université Montpellier
936 II. p. 244.
- 937 48. Arena, H., et al., *Impact of Zn, Mg, Ni and Co elements on glass alteration: Additive effects*.
938 Journal of Nuclear Materials, 2016. **470**: p. 55-67.

- 939 49. Aréna, H., et al., *Impact of iron and magnesium on glass alteration: Characterization of the*
940 *secondary phases and determination of their solubility constants*. Applied Geochemistry, 2017.
941 **82**: p. 119-133.
- 942 50. Aréna, H., et al., *Impact of Fe, Mg and Ca elements on glass alteration: Interconnected processes*.
943 *Geochimica et Cosmochimica Acta*, 2018. **239**: p. 420-445.
- 944 51. Mercado-Depierre, S., et al., *Antagonist effects of calcium on borosilicate glass alteration*.
945 *Journal of Nuclear Materials*, 2013. **441**(1-3): p. 402-410.
- 946 52. Jollivet, P., et al., *Effect of clayey groundwater on the dissolution rate of the simulated nuclear*
947 *waste glass SON68*. *Journal of Nuclear Materials*, 2012. **420**: p. 508-518.
- 948 53. Jegou, C., S. Gin, and F. Larche, *Alteration kinetics of a simplified nuclear glass in an aqueous*
949 *medium: effects of solution chemistry and of protective gel properties on diminishing the*
950 *alteration rate*. *Journal of Nuclear Materials*, 2000. **280**(2): p. 216-229.
- 951 54. Gin, S., et al., *Effect of composition on the short-term and long-term dissolution rates of ten*
952 *glasses of increasing complexity from 3 to 30 oxides*. *Journal of Non-Crystalline Solids*, 2012.
953 **358**(18-19): p. 2559-2570.
- 954 55. Gin, S., Abdelouas, A., Criscenti, L.J., Ebert, W.L., Ferrand, K., Geisler, T., Harrison, M.T., Inagaki,
955 Y., Mitsui, S., Mueller, K.T., Marra, J.C., Pantano, C.G., Pierce, E.M., Ryan, J.V., Schofield, J.M.,
956 Steefel, C.I., Vienna, J.D., *An international initiative on long-term behavior of high-level nuclear*
957 *waste glass*. *Materials Today*, 2013. **16**(6): p. 243-248.
- 958 56. Trotignon, L., et al., *The compared aqueous corrosion of four simple borosilicate glasses:*
959 *Influence of Al, Ca, and Fe on the formation and nature of secondary phases*. *Journal of Nuclear*
960 *Materials*, 1992. **190**: p. 228-246.
- 961 57. Neeway, J., *The alteration of the SON68 reference waste glass in silica saturated conditions and*
962 *in the presence of water vapor*. 2010, Université de Nantes. p. 205.
- 963 58. Bouakkaz, R., *Altération aqueuse et hydratation en phase vapeur du verre SON68 à basse*
964 *température (35-90°C)*. 2014, L'Université Nantes Angers Le Mans.
- 965 59. Peña, F.d.l., et al., *hyperspy/hyperspy v1.4.1*. 2018.
- 966 60. Collin, M., et al., *Impact of alkali on the passivation of silicate glass*. *npj Materials Degradation*,
967 2018. **2**(1): p. 16.
- 968 61. Angeli, F., et al., *Structure and Chemical Durability of Lead Crystal Glass*. *Environmental Science*
969 *& Technology*, 2016. **50**(21): p. 11549-11558.
- 970 62. Spalla, O., S. Lyonard, and F. Testard, *Analysis of the small-angle intensity scattered by a porous*
971 *and granular medium*. *Journal of Applied Crystallography*, 2003. **36 part 32**: p. 338-347.
- 972 63. Spalla, O., et al., *Influence of insoluble elements on the nanostructure of water altered glasses*.
973 *Journal of Non-Crystalline Solids*, 2004. **347**(1-3): p. 56-68.
- 974 64. Cailleteau, C., *Influence de la morphologie du gel sur la cinétique d'altération des verres*
975 *nucléaires: rôle du calcium et du zirconium*. 2008, Thèse de l'école polytechnique de Paris.
- 976 65. Thien, B.M.J., *A simple way to constrain the stoichiometry of secondary smectites upon aqueous*
977 *glass alteration*. *Applied Geochemistry*, 2014. **42**: p. 45-46.
- 978 66. Jolyon, R. and I. Chau, *Mindat : base de données minéralogiques*, in <http://www.mindat.org/>.
979 2013.
- 980 67. Bailey, S.W., *Crystal Structures of Clay Minerals and Their X-ray Identification*. Mineralogical
981 Society, London, 1980. **Monograph 5**: p. 1-123.
- 982 68. Brindley, G.W. and G. Brown, *Crystal Structures of Clay Minerals and their X-ray identification*.
983 Mineralogical Society, London, 1980. **Monograph 5**: p. 169-180.
- 984 69. Klopogge, J.T., S. Komarneni, and J.E. Amonette, *Synthesis of smectite clay minerals a critical*
985 *review*. *Clays and Clay Minerals*, 1999. **47**(5): p. 529-554.

- 986 70. Harder, H., *The role of magnesium in the formation of smectite minerals*. Chemical Geology,
987 1972. **10**(1): p. 31-39.
- 988 71. Pascua, C.S. and H. Yamada, *LOW-TEMPERATURE FORMATION OF CLAY MINERALS :
989 CORRELATING LABORATORY EXPERIMENTS WITH NATURAL FIELD-SCALE PROCESSES*. Clay
990 Science, 2012. **16**(2): p. 25-32.
- 991 72. Joly, J.-F., et al., *Phyllosilicates 2:1 trioctaédriques et leur procédé de préparation*, E.P. Office,
992 Editor. 1991, IFP Energies Nouvelles France.
- 993 73. Py, M., *Study of interfaces and nanometric structures by ToF-SIMS : upon a spatially resolved
994 quantitative analysis*, in *Micro and nanotechnologies/Microelectronics*. 2011, Université de
995 Grenoble.
- 996 74. Romanos, G.E., et al., *Methods of evaluating pore morphology in hybrid organic–inorganic
997 porous materials*. Microporous and Mesoporous Materials, 2009. **120**(1): p. 53-61.
- 998 75. Alloteau, F., *Contribution à la compréhension des mécanismes de l'altération atmosphérique des
999 verres et étude d'un traitement de protection à base de sels de zinc. Application à la conservation
1000 des objets en verre du patrimoine culturel*. 2017, l'Université de recherche Paris Sciences et
1001 Lettres PSL Research University.
- 1002 76. Biron, I., *Émaux sur Métal – du IXe au XIXe Siècle. Histoire, Technique et Matériaux*. 2015: Faton
1003 edition.
- 1004 77. Sterpenich, J. and G. Libourel, *Using stained glass windows to understand the durability of toxic
1005 waste matrices*. Chemical Geology, 2001. **174**: p. 181-193.
- 1006 78. France Commissariat à l'énergie, a., V. Centre de, and I.I.S.e.t.d.L. Université Montpellier, *Actes
1007 des journées sur le Verre: Université d'été CEA/VALRHÔ = CEA/VALRHÔ Summer Session
1008 proceedings Glass ; Recherche scientifique pour un confinement de haute performance =
1009 Scientific research for high performance containment, 31 août-7 septembre 1997 = 31 august-7
1010 september 1997, Méja*. Commissariat à l'énergie atomique 1997.
- 1011 79. Sterpenich, J., *Altération des vitraux médiévaux - Contribution à l'étude du comportement à long
1012 terme des verres de confinement*. 1998, Université Henri Poincaré. p. 440.
- 1013 80. Barger, M.S., D.K. Smith, and W.B. White, *Characterization of corrosion products on old
1014 protective glass, especially daguerreotype cover glasses*. Journal of Materials Science, 1989.
1015 **24**(4): p. 1343-1356.
- 1016 81. Rebiscoul, D., et al., *Protective properties and dissolution ability of the gel formed during nuclear
1017 glass alteration*. Journal of Nuclear Materials, 2005. **342**(1): p. 26-34.
- 1018 82. Rebiscoul, D., et al., *Morphological evolution of alteration layers formed during nuclear glass
1019 alteration: new evidence of a gel as a diffusive barrier*. Journal of Nuclear Materials, 2004.
1020 **326**(1): p. 9-18.
- 1021 83. Cailleteau, C., et al., *Why Do Certain Glasses with a High Dissolution Rate Undergo a Low Degree
1022 of Corrosion?* The Journal of Physical Chemistry C, 2011. **115**(13): p. 5846-5855.
- 1023 84. Le Guillou, C., et al., *New experimental approach to study aqueous alteration of amorphous
1024 silicates at low reaction rates*. Chemical Geology, 2015. **412**: p. 179-192.
- 1025 85. Balasubramanian, R., et al., *Investigation of the vaporization of boric acid by transpiration
1026 thermogravimetry and knudsen effusion mass spectrometry*. J. Phys. Chem. B, 2008. **112**: p.
1027 13873-13884.
- 1028 86. Gaillardet, J., et al., *Evaporation and Sublimation of Boric Acid: Application for Boron Purification
1029 from Organic Rich Solutions*. Geostandards Newsletter, 2001. **25**(1): p. 67-75.
- 1030 87. Siboni, S. and C. Della Volpe, *Some mathematical aspects of the Kelvin equation*. Computers &
1031 Mathematics with Applications, 2008. **55**(1): p. 51-65.
- 1032 88. Sicard, L., et al., *Study of the kinetics of glass alteration by small-angle X-ray scattering*. Journal
1033 of Physical Chemistry B, 2004. **108**: p. 7702-7708.

- 1034 89. Girard, L., M. Arab, and O. Spalla, *Time resolved alteration process of oxide glasses*. Journal of
 1035 Colloid and Interface Science, 2008. **319**(1): p. 214-225.
- 1036 90. Toquer, G., et al., *Effect of leaching concentration and time on the morphology of pores in porous*
 1037 *glasses*. Journal of Non-Crystalline Solids, 2011. **357**(6): p. 1552-1557.
- 1038 91. Kanehashi, K., *Structural roles of calcium in alkaline and alkaline-earth aluminosilicate glasses by*
 1039 *solid-state ^{43}Ca , ^{17}O and ^{27}Al NMR*. Solid State Nuclear Magnetic Resonance, 2017. **84**: p. 158-
 1040 163.
- 1041 92. Guo, R., et al., *The effect of magnesium on the local structure and initial dissolution rate of*
 1042 *simplified UK Magnox waste glasses*. Journal of Non-Crystalline Solids, 2018. **497**: p. 82-92.
- 1043 93. Angeli, F., et al., *Influence of glass composition and alteration solution on leached silicate glass*
 1044 *structure : a solid-state NMR investigation*. Geochimica et Cosmochimica Acta, 2006. **70**(10): p.
 1045 2577-2590.
- 1046 94. Thien, B., et al., *Structural identification of a trioctahedral smectite formed by the aqueous*
 1047 *alteration of a nuclear glass*. Applied Clay Science, 2010. **49**: p. 135-141.
- 1048 95. Sicard, L., et al., *Dissolution of Oxide Glasses: A Process Driven by Surface Generation*. The
 1049 Journal of Physical Chemistry C, 2008. **112**(5): p. 1594-1603.
- 1050 96. Pons-Corbeau, J., et al., *Quantitative Surface Analysis by Glow Discharge Optical Spectrometry*.
 1051 Surface and interface analysis, 1986. **9**: p. 21-25.

1052

1053 Tables and figures

1054 List of Figures

- 1055 Figure 1 (a) SEM image (cross-section) of AVM6 (altered for 180 days at 50°C and 95%RH) showing an
 1056 irregularly altered zone; (b) TEM image of AVM6 (cross-section) (altered for 557 days) showing a porous
 1057 irregularly altered zone on the left side of the image and an unaltered zone adjacent to it. (from top) the
 1058 resin, the layer of phyllosilicates of approx. 200-250 nm thickness, a homogeneous gel layer of approx.
 1059 70 nm thickness and the very porous altered zone. The pores visible beneath the homogeneous gel layer
 1060 on the right side of the image were enlarged due to exposure to electron beam; but this clearly shows
 1061 the presence of the homogeneous gel layer even in zones where irregular altered zone is not present; (c)
 1062 SEM image of AVM10 (cross-section) (altered for 180 days) showing an irregularly altered zone; (d)
 1063 STEM-BF image of AVM10 (cross-section) (altered for 557 days). This micro-section shows one irregularly
 1064 altered zone spanning approx. 230 nm and the presence of a uniform approx. 30 nm thick gel layer
 1065 throughout the micro-section 36
- 1066 Figure 2 (a) SEM image of AVM6 (altered for 180 days at 50°C and 95% RH) showing leafy precipitates
 1067 and needle shaped crystalline phases; (b) TEM image of AVM6 (cross-section) (altered for 180 days)
 1068 showing a 70 nm thick layer of phyllosilicates above an approx. 50 nm thick homogeneous gel layer. The
 1069 porous irregularly altered zone is present beneath the homogeneous gel layer; (c) SEM image of AVM6
 1070 (altered for 557 days) - Formation of crystalline precipitates along straight lines assumed to be surface
 1071 defects created while polishing; (d) Closer look at image (c) – Cluster of needle shape precipitates; (e)
 1072 TEM image of AVM10 (cross-section) (altered for 180 days) - The image shows the presence of poorly
 1073 crystallized phyllosilicates of approx. 330 nm thickness at the surface; the black circular spots are

1074	precipitates rich in Ag, Mo and P. Beneath the precipitates, a uniform gel layer of 15-30 nm is present. A	
1075	very porous altered zone is present beneath the homogeneous gel layer; (f) TEM image of AVM10 (cross-	
1076	section) (altered for 557 days) – The image shows the presence of well-developed approx. 70 nm thick	
1077	phyllosilicate layer containing precipitates rich in Ag, Mo and P (circular spots). Underneath, an approx.	
1078	27 nm thick uniform gel layer is present. The porosity visible at the gel-glass interface is an artificial	
1079	enlargement of pores due to exposure to electron beam.....	37
1080	Figure 3 (a) SEM image of QMg (altered for 180 days at 50°C and 95% RH) showing a carpet of thread-like	
1081	precipitate and fibrous cluster of secondary precipitates; (b) SEM image of QMg (altered for 557 days)	
1082	showing a gnawed appearance at the altered sample surface; (c) SEM image of AVMV4 (altered for 180	
1083	days) showing a similar altered surface to QMg altered for the same duration; (d) SEM image of AVMV4	
1084	(altered for 557 days) showing holes/pits of size 400-500 nm; (e) TEM image of AVMV4-557 (cross-	
1085	section) showing a layer of phyllosilicates of varying thickness on altered glass surface and a uniform	
1086	homogeneous gel layer of approx. 80 nm thickness; (f) A zoom of image (e), showing the homogeneous	
1087	gel layer with a mixture of amorphous and crystalline precipitates on the altered surface. There appear	
1088	to be more crystallized precipitates towards the surface and at the interface of gel-layer precipitate-layer	
1089	38
1090	Figure 4 (a) STEM image of QMg (cross-section) (altered for 180 days at 50°C and 95% RH); (b) TEM	
1091	image of Q (cross-section) (altered for 180 days)	39
1092	Figure 5 (a) TEM image of QCa (cross-section) altered for 180 days at 50°C and 95% RH; (b) SEM image of	
1093	QCa altered for 557 days at 50°C and 95% RH; (c) SEM image of cross-section of QCa altered for 557 days	
1094	39
1095	Figure 6 ToF-SIMS profiles of all six glasses altered at 50°C and 95% RH for 180 days; The profiles of only	
1096	the major elements of the AVM glasses are shown here	40
1097	Figure 7 SAXS spectra of the glasses (a) Q and (b) QCa that were unaltered (black squares), altered for	
1098	180 days (blue circles) and 557 days (orange triangles); The red dotted lines represent $I \propto q^{-4}$; The inset	
1099	graphs show the plot of $(I(\text{corr}) * q^4)$ vs. q highlighting the shift of the porod regime towards lower q with	
1100	increasing duration of alteration; $I(\text{corr})$ is a result of data treatment to separate the intensity scattered	
1101	by grain envelopes and the inner pores of the gel layer	41
1102	Figure 8 Evolution of $(A-A_0)$ with time; (i. e.) The increase in the absorbance of the SiOH band at 3600 cm^{-1}	
1103	of deconvoluted FTIR spectra of glasses altered at 50°C and 95% RH until 557 days (A) with respect to	
1104	the absorbance of the SiOH band of the deconvoluted FTIR spectrum of the unaltered glass monolith	
1105	(A_0) . (a) Evolution of $(A-A_0)$ for all six glasses; (b) Evolution of $(A-A_0)$ of the glasses Q and QCa; (c)	
1106	Evolution of $(A-A_0)$ of the glasses AVMV4 and QMg; (d) A zoom of image (a) to observe closely the	
1107	evolution of $(A-A_0)$ of AVM10 glass until 180 days.....	42
1108	Figure 9 (a) Description of the altered layer morphology of the six glasses that were vapor hydrated at	
1109	50°C and 95%RH for 180 days and 557 days; This description was constructed based on TEM images and	
1110	ToF-SIMS profiles at 557 days; X-axis is the mol% of elements (without considering O) calculated from	
1111	ToF-SIMS intensities based on Pons-Corbeau method ([96]); y-axis is the distance from the surface in nm;	
1112	The portions of the ToF-SIMS profiles that correspond to pristine glass, homogeneous gel layer and	
1113	smectites were chosen approximatively by a combined analysis of TEM images and ToF-SIMS profiles; (b)	
1114	Schematic description of the morphology of the altered glasses	43
1115		

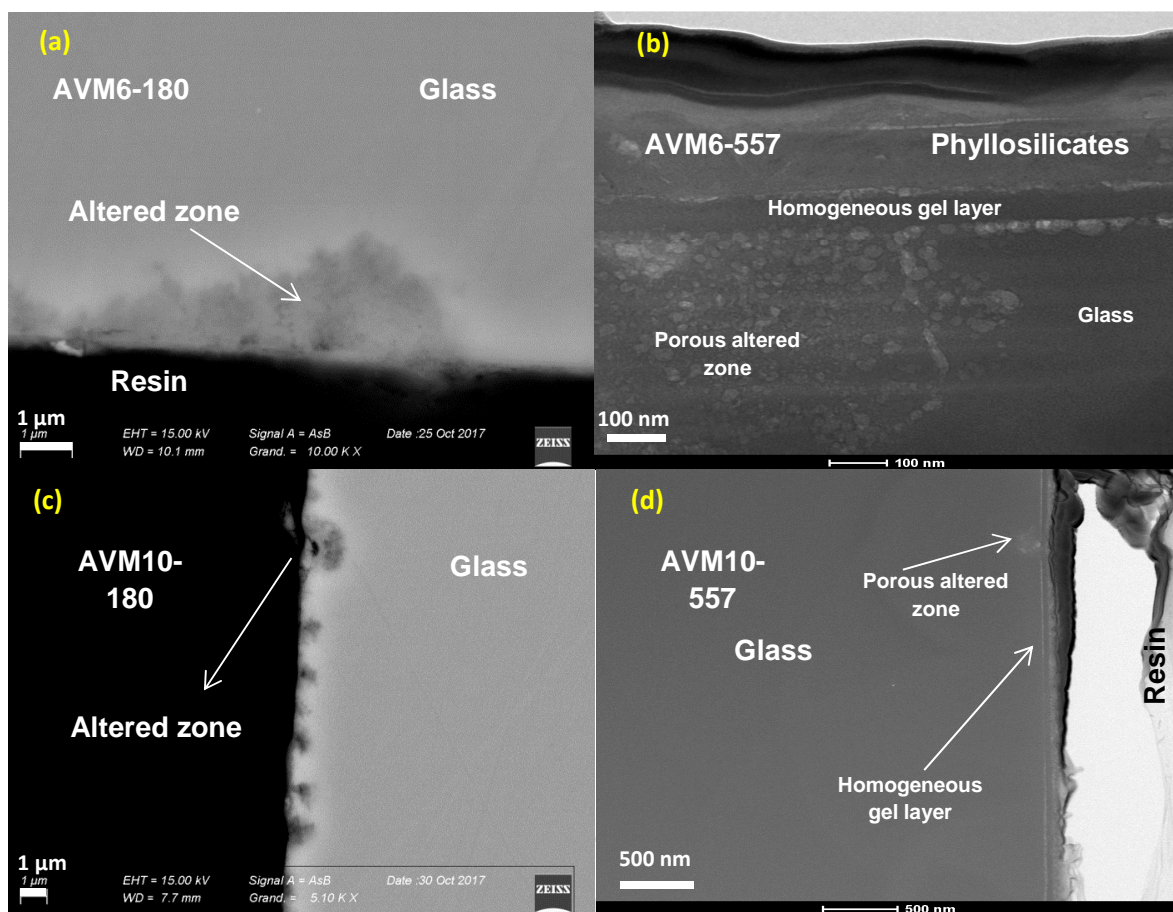
1116 List of tables

1117	Table 1 Glass compositions (mol% of oxides) (measured by ICP) (error 3%) and fraction of Non-	
1118	Bridging Oxygen atoms (NBO) and percent of boron in 4-coordination (^{IV} B) (error 3-8%).....	44
1119	Table 2 Composition (normalized to 4 moles of Si) of phyllosilicates measured by STEM-EDX analyses (at	
1120	least 12% relative error).....	45
1121	Table 3 Thickness (in nm) of the altered layer (altered at 50°C and 95% RH for 180 days and 557 days	
1122	each); (ToF-SIMS) is measured from equation 2.4.4.2; (TEM) is measured based on the density difference	
1123	between pristine glass and gel layer in TEM images.....	45
1124	Table 4 Porosity, pore-size and surface area of gel calculated from SAXS data; ϕ_{gel} corresponds to the	
1125	volume fraction of gel calculated from ToF-SIMS profiles of monoliths that were used to calculate the	
1126	porosity of the gel formed on glass powders.....	46
1127		

1128

1129

1130



1131

1132

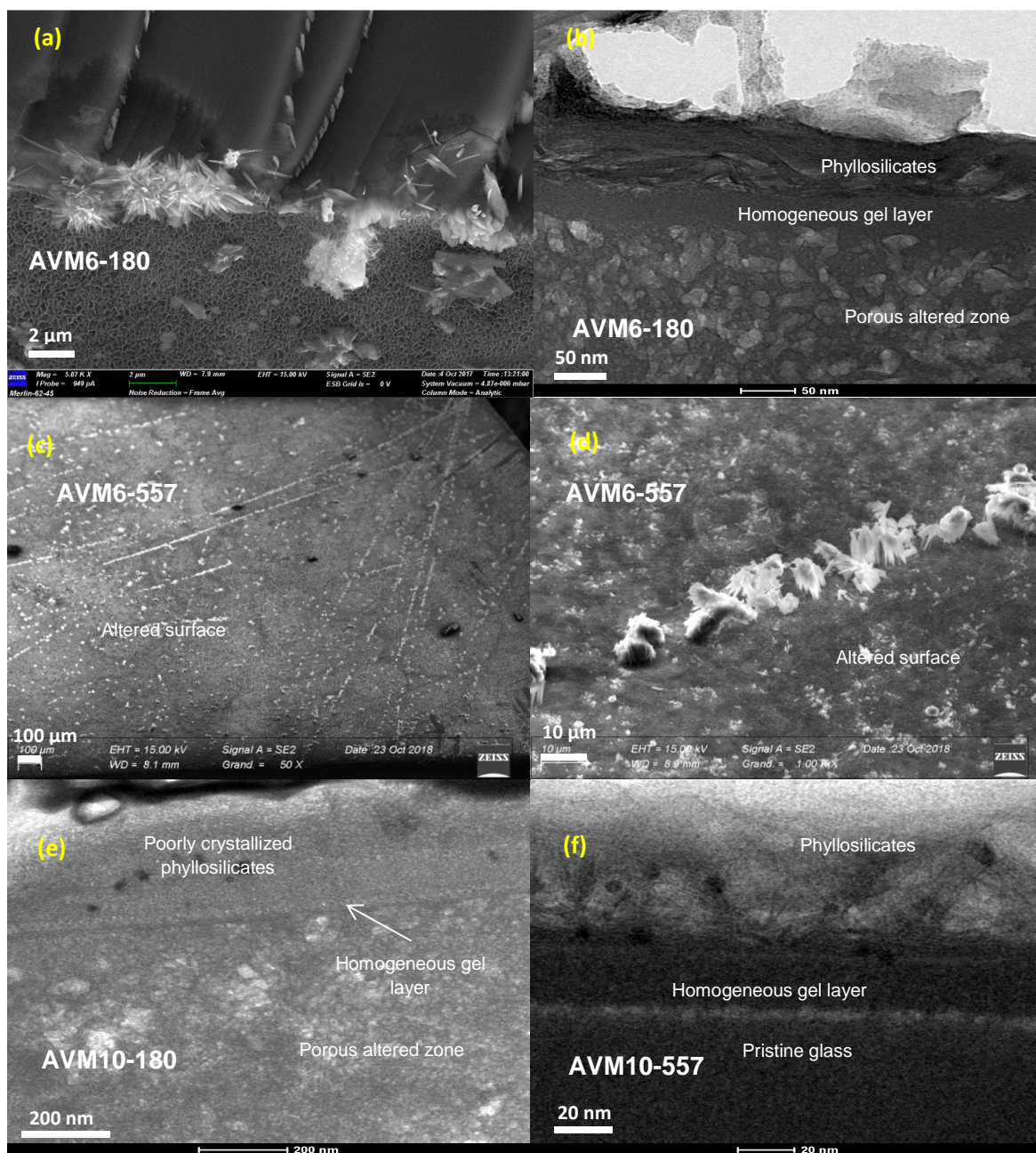
1133 *Figure 1 (a) SEM image (cross-section) of AVM6 (altered for 180 days at 50°C and 95%RH) showing an irregularly altered zone;*
 1134 *(b) TEM image of AVM6 (cross-section) (altered for 557 days) showing a porous irregularly altered zone on the left side of the*
 1135 *image and an unaltered zone adjacent to it. (from top) the resin, the layer of phyllosilicates of approx. 200-250 nm thickness, a*
 1136 *homogeneous gel layer of approx. 70 nm thickness and the very porous altered zone. The pores visible beneath the homogeneous*
 1137 *gel layer on the right side of the image were enlarged due to exposure to electron beam; but this clearly shows the presence of*
 1138 *the homogeneous gel layer even in zones where irregular altered zone is not present; (c) SEM image of AVM10 (cross-section)*
 1139 *(altered for 180 days) showing an irregularly altered zone; (d) STEM-BF image of AVM10 (cross-section) (altered for 557 days).*
 1140 *This micro-section shows one irregularly altered zone spanning approx. 230 nm and the presence of a uniform approx. 30 nm*
 1141 *thick gel layer throughout the micro-section*

1142

1143

1144

1145



1146

1147

1148

1149

1150

1151

1152

1153

1154

1155

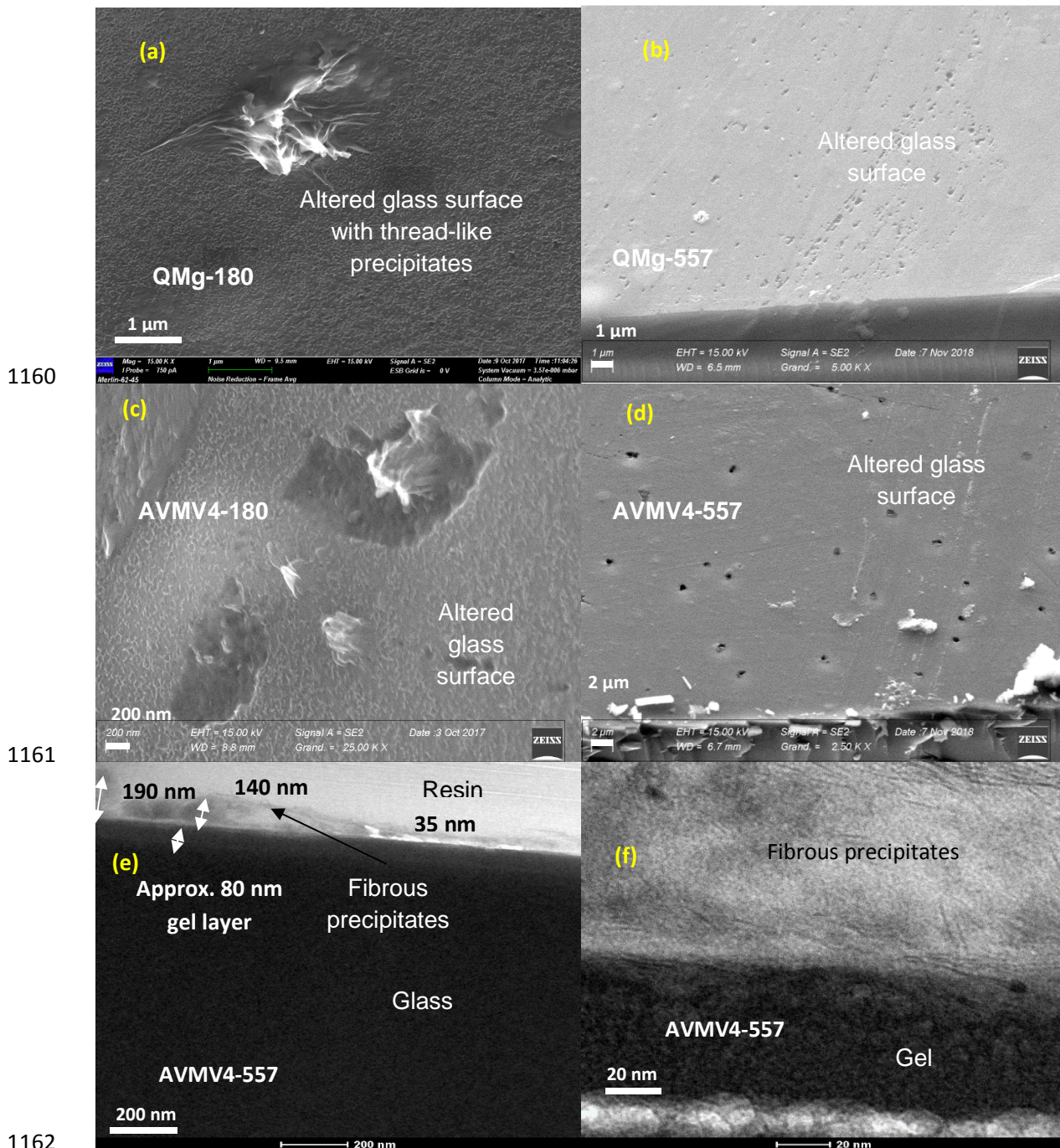
1156

1157

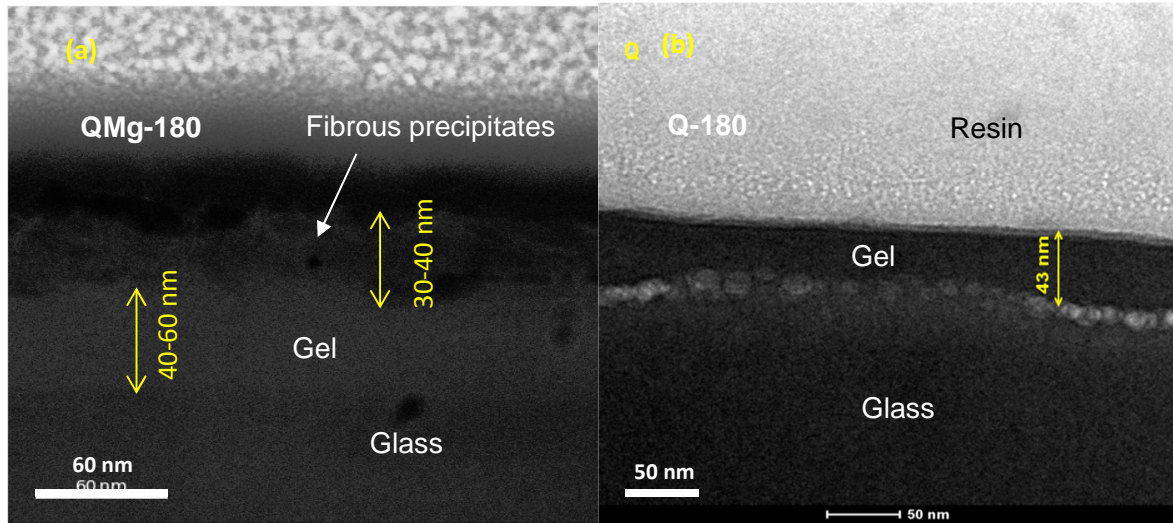
1158

1159

Figure 2 (a) SEM image of AVM6 (altered for 180 days at 50°C and 95% RH) showing leafy precipitates and needle shaped crystalline phases; (b) TEM image of AVM6 (cross-section) (altered for 180 days) showing a 70 nm thick layer of phyllosilicates above an approx. 50 nm thick homogeneous gel layer. The porous irregularly altered zone is present beneath the homogeneous gel layer; (c) SEM image of AVM6 (altered for 557 days) - Formation of crystalline precipitates along straight lines assumed to be surface defects created while polishing; (d) Closer look at image (c) – Cluster of needle shape precipitates; (e) TEM image of AVM10 (cross-section) (altered for 180 days) - The image shows the presence of poorly crystallized phyllosilicates of approx. 330 nm thickness at the surface; the black circular spots are precipitates rich in Ag, Mo and P. Beneath the precipitates, a uniform gel layer of 15-30 nm is present. A very porous altered zone is present beneath the homogeneous gel layer; (f) TEM image of AVM10 (cross-section) (altered for 557 days) – The image shows the presence of well-developed approx. 70 nm thick phyllosilicate layer containing precipitates rich in Ag, Mo and P (circular spots). Underneath, an approx. 27 nm thick uniform gel layer is present. The porosity visible at the gel-glass interface is an artificial enlargement of pores due to exposure to electron beam.

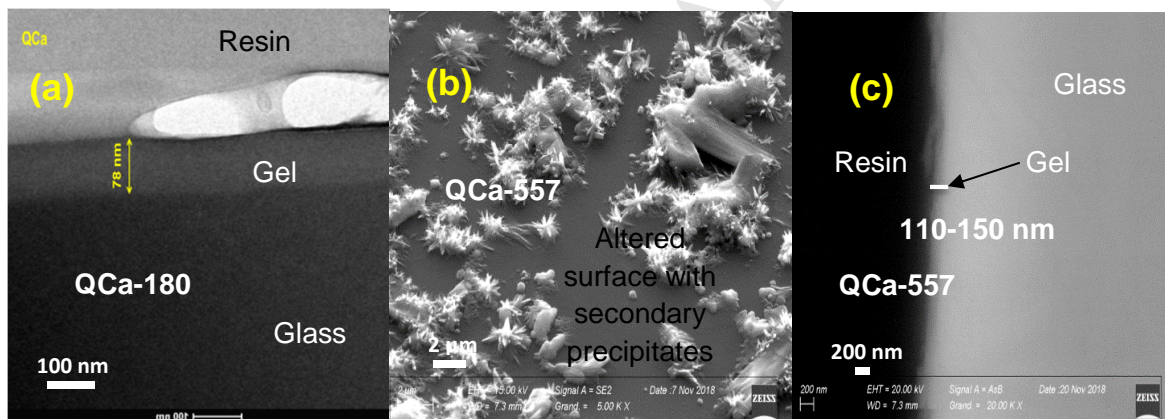


1163 *Figure 3 (a) SEM image of QMg (altered for 180 days at 50°C and 95% RH) showing a carpet of thread-like precipitate and fibrous*
 1164 *cluster of secondary precipitates; (b) SEM image of QMg (altered for 557 days) showing a gnawed appearance at the altered*
 1165 *sample surface; (c) SEM image of AVMV4 (altered for 180 days) showing a similar altered surface to QMg altered for the same*
 1166 *duration; (d) SEM image of AVMV4 (altered for 557 days) showing holes/pits of size 400-500 nm; (e) TEM image of AVMV4-557*
 1167 *(cross-section) showing a layer of phyllosilicates of varying thickness on altered glass surface and a uniform homogeneous gel*
 1168 *layer of approx. 80 nm thickness; (f) A zoom of image (e), showing the homogeneous gel layer with a mixture of amorphous and*
 1169 *crystalline precipitates on the altered surface. There appear to be more crystallized precipitates towards the surface and at the*
 1170 *interface of gel-layer precipitate-layer*



1171
 1172 *Figure 4 (a) STEM image of QMg (cross-section) (altered for 180 days at 50°C and 95% RH); (b) TEM image of Q (cross-section)*
 1173 *(altered for 180 days)*

1174



1175
 1176 *Figure 5 (a) TEM image of QCa (cross-section) altered for 180 days at 50°C and 95% RH; (b) SEM image of QCa altered for 557*
 1177 *days at 50°C and 95% RH; (c) SEM image of cross-section of QCa altered for 557 days*

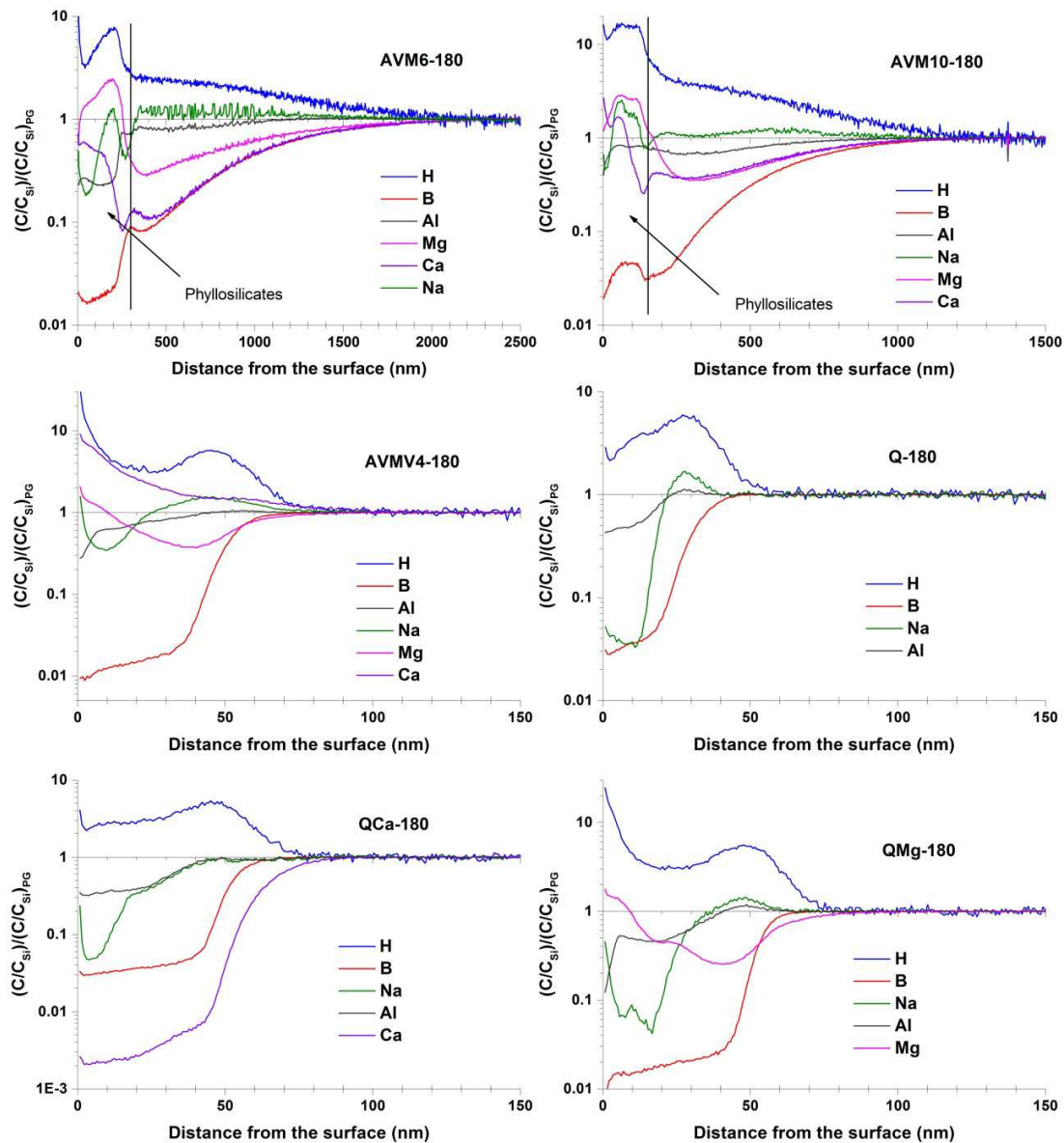
1178

1179

1180

1181

1182



1183

1184 *Figure 6 ToF-SIMS profiles of all six glasses altered at 50°C and 95% RH for 180 days; The profiles of only the major elements of*
 1185 *the AVM glasses are shown here*

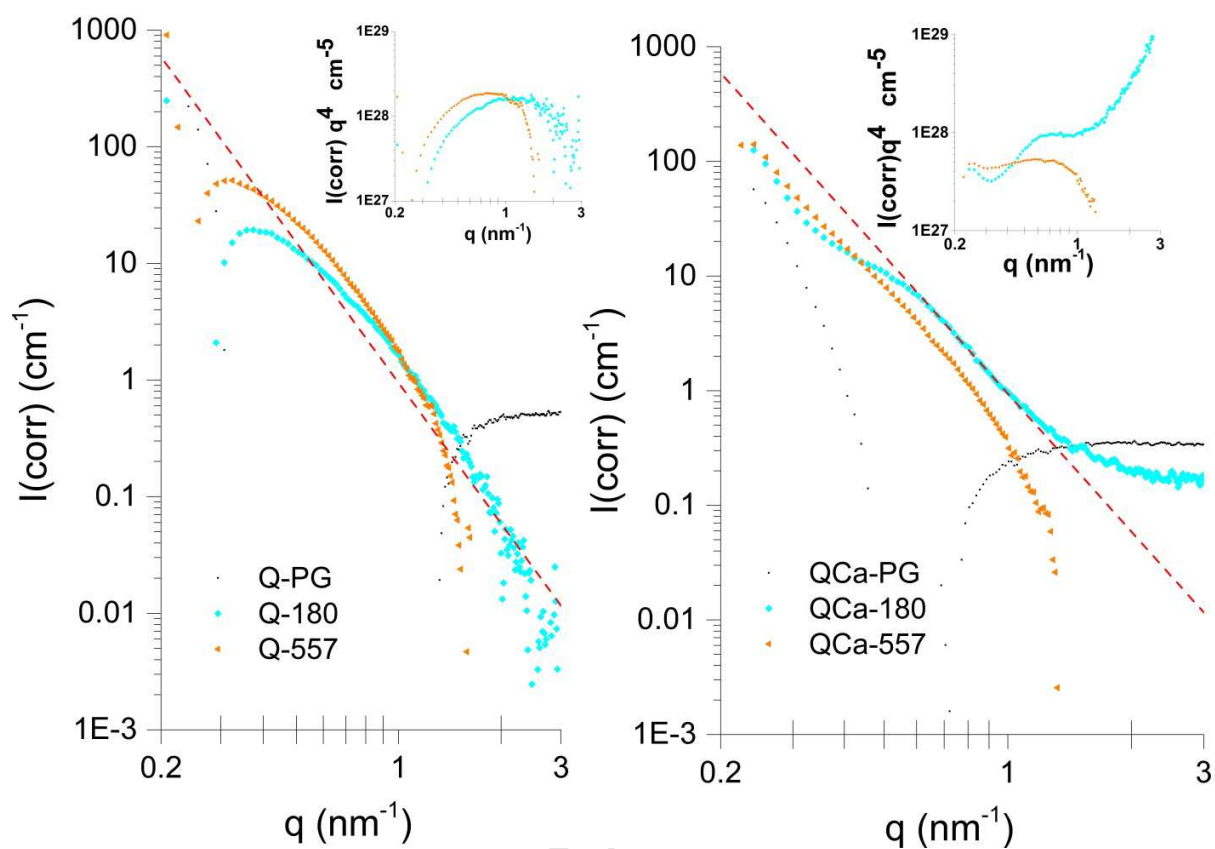
1186

1187

1188

1189

1190

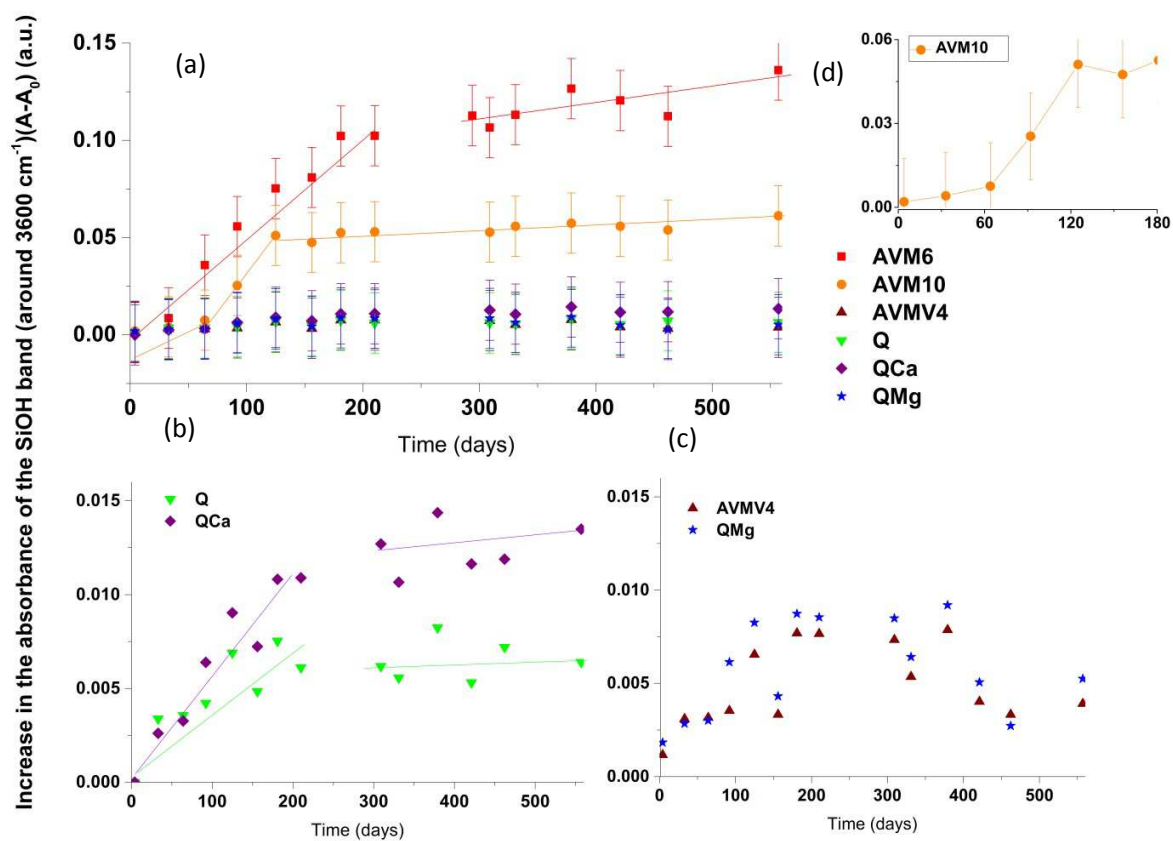


1191

1192 Figure 7 SAXS spectra of the glasses (a) Q and (b) QCa that were unaltered (black squares), altered for 180 days (blue circles) and
 1193 557 days (orange triangles); The red dotted lines represent $I \propto q^{-4}$; The inset graphs show the plot of $(I(\text{corr}) * q^4)$ vs. q highlighting
 1194 the shift of the porod regime towards lower q with increasing duration of alteration; $I(\text{corr})$ is a result of data treatment to
 1195 separate the intensity scattered by grain envelopes and the inner pores of the gel layer

1196

1197



1198

1199 *Figure 8 Evolution of $(A-A_0)$ with time; (i. e.) The increase in the absorbance of the SiOH band at 3600 cm⁻¹ of deconvoluted FTIR*
 1200 *spectra of glasses altered at 50°C and 95% RH until 557 days (A) with respect to the absorbance of the SiOH band of the*
 1201 *deconvoluted FTIR spectrum of the unaltered glass monolith (A_0). (a) Evolution of $(A-A_0)$ for all six glasses; (b) Evolution of $(A-A_0)$*
 1202 *of the glasses Q and QCa; (c) Evolution of $(A-A_0)$ of the glasses AVMV4 and QMg; (d) A zoom of image (a) to observe closely the*
 1203 *evolution of $(A-A_0)$ of AVM10 glass until 180 days*

1204

1205

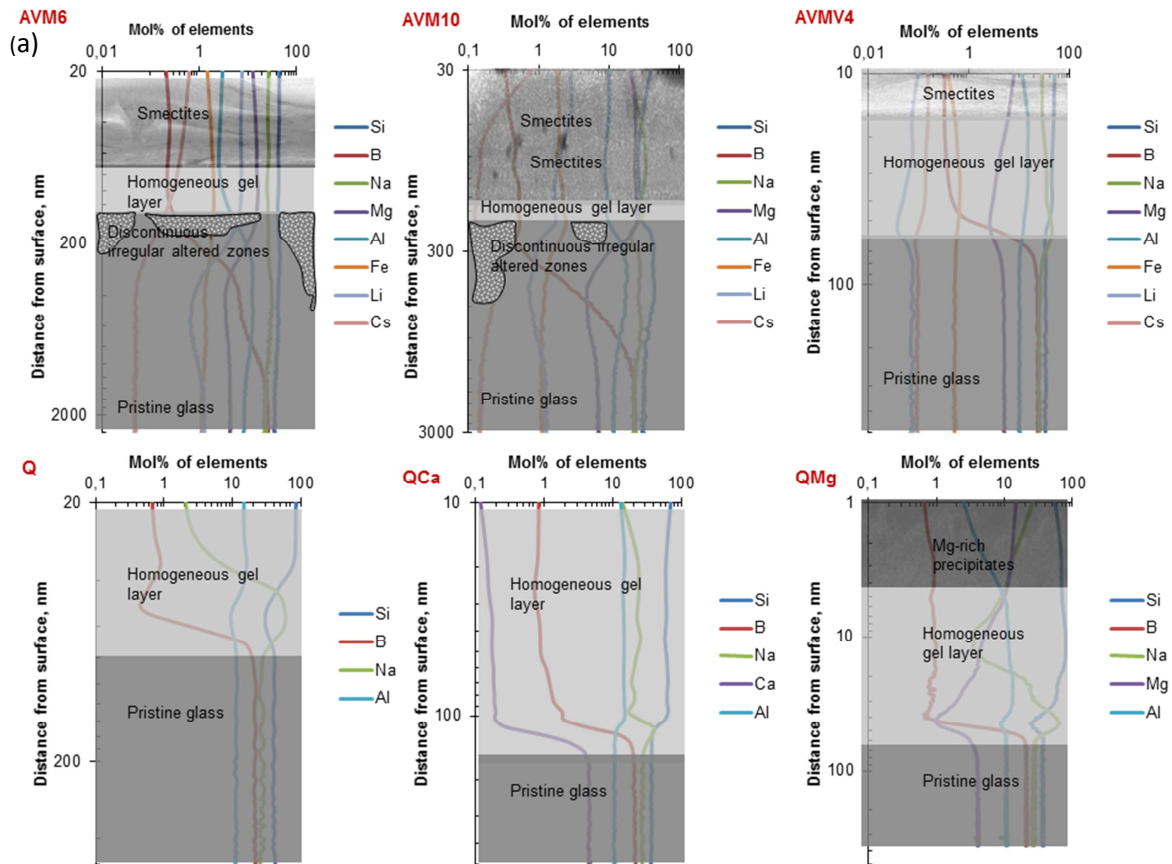
1206

1207

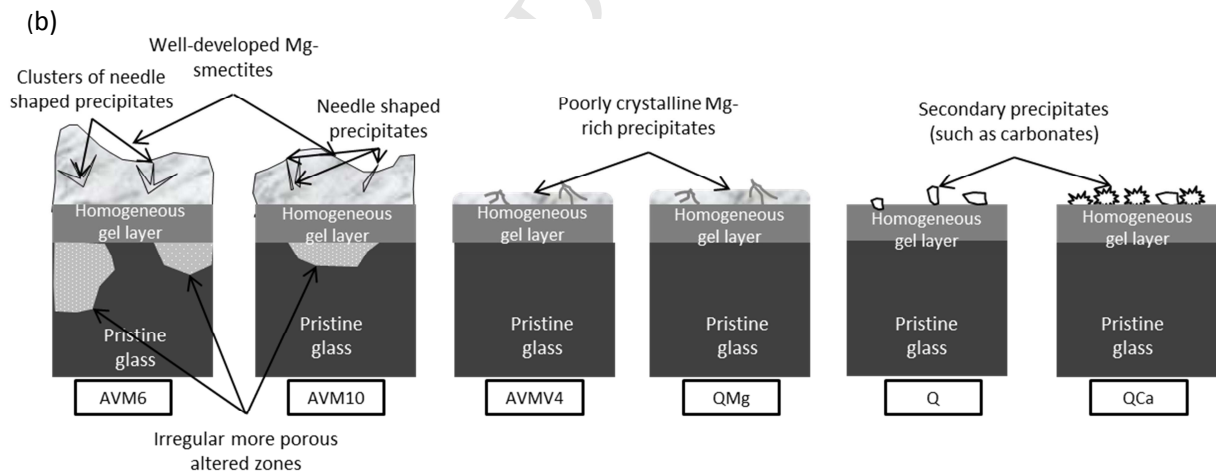
1208

1209

1210



1211



1212

1213 Figure 9 (a) Description of the altered layer morphology of the six glasses that were vapor hydrated at 50°C and 95%RH for 180
 1214 days and 557 days; This description was constructed based on TEM images and ToF-SIMS profiles at 557 days; X-axis is the mol%
 1215 of elements (without considering O) calculated from ToF-SIMS intensities based on Pons-Corbeau method ([96]); y-axis is the
 1216 distance from the surface in nm; The portions of the ToF-SIMS profiles that correspond to pristine glass, homogeneous gel layer
 1217 and smectites were chosen approximatively by a combined analysis of TEM images and ToF-SIMS profiles; (b) Schematic
 1218 description of the morphology of the altered glasses

1219

1220 *Table 1 Glass compositions (mol% of oxides) (measured by ICP) (error 3%) and fraction of Non-Bridging Oxygen*
 1221 *atoms (NBO) and percent of boron in 4-coordination (^{IV}B) (error 3-8%)*

	AVMV4	AVM6	AVM10	Q	QCa	QMg
SiO₂	48.16	49.29	43.39	57.48	52.67	52.6
Al₂O₃	7.15	5.88	8.30	8.07	7.49	7.74
B₂O₃	16.71	18.64	16.29	15.28	14.6	15.02
Na₂O	18.61	16.65	16.39	19.17	19.01	18.83
CaO	0.04	0.24	0.24	0	6.23	0
MgO	7.15	6.28	10.38	0	0	5.81
Li₂O	0.05	0.89	0.91	0	0	0
ZrO₂	0.22	0.10	0.29	0	0	0
Fe₂O₃	0.38	0.79	0.81	0	0	0
NiO	0.13	0.27	0.27	0	0	0
Cr₂O₃	0.09	0.20	0.20	0	0	0
P₂O₅	0.08	0.00	0.81	0	0	0
SrO	0.06	0.03	0.08	0	0	0
Y₂O₃	0.02	0.01	0.02	0	0	0
MoO₃	0.29	0.13	0.39	0	0	0
MnO	0.10	0.05	0.13	0	0	0
Ag₂O	0.02	0.01	0.03	0	0	0
CdO	0.05	0.26	0.26	0	0	0
TeO₂	0.03	0.01	0.03	0	0	0
Cs₂O	0.07	0.03	0.09	0	0	0
BaO	0.06	0.03	0.08	0	0	0
La₂O₃	0.05	0.02	0.06	0	0	0
Ce₂O₃	0.05	0.02	0.07	0	0	0
Pr₂O₃	0.02	0.01	0.03	0	0	0
Nd₂O₃	0.14	0.04	0.10	0	0	0
RuO₂	0.17	0.08	0.22	0	0	0
PdO	0.11	0.05	0.15	0	0	0
Fraction of NBO	0.134	0.158	0.162	0.036	0.111	0.115
Percent of ^{IV}B	39	20	27	48.5	46.5	37

1222

1223

1224

1225 Table 2 Composition (normalized to 4 moles of Si) of phyllosilicates measured by STEM-EDX analyses (at least 12% relative error)

	O	Mg	Al	Si	Ca	Cr	Fe	Nd	
AVM6-180	13.60	1.51	0.18	4.00	0.07	0.01	0.18	0.01	
AVM6-557	15.62	1.72	0.20	4.00	0.06	0.03	0.16	0.00	
	O	Mg	Al	Si	P	Ca	Cr	Fe	Nd
AVM10-180	35.00	3.44	1.09	4.00	0.21	0.10	0.00	0.27	0.08
AVM10-557	20.82	2.01	1.06	4.00	0.17	0.16	0.01	0.23	0.00

1226

1227 Table 3 Thickness (in nm) of the altered layer (altered at 50°C and 95% RH for 180 days and 557 days each); (ToF-SIMS) is
1228 measured from equation 2.4.4.2; (TEM) is measured based on the density difference between pristine glass and gel layer in TEM
1229 images

Duration of alteration	180 days		557 days	
	(ToF-SIMS)	(TEM)	(ToF-SIMS)	(TEM)
AVM6	1060	(70 nm homogeneous layer + Irregular alteration + surface precipitates)	900	(70 nm homogeneous layer + Irregular alteration + surface precipitates)
AVM10	630	(~30 nm homogeneous layer + Irregular alteration + surface precipitates)	905	(~30 nm homogeneous layer + Irregular alteration + surface precipitates)
AVMV4	52	-	64	(~80 nm homogeneous altered layer + surface precipitates)
Q	31	~43 nm homogeneous altered layer	66	~76 nm homogeneous altered layer
QCa	52	~78 nm homogeneous altered layer	121	110-150 nm homogeneous altered layer (SEM)
QMg	53	(~60 nm altered layer + ~30 nm fibrous precipitates)	66	(~76 nm homogeneous altered layer + surface precipitates)

1230

1231

1232 *Table 4 Porosity, pore-size and surface area of gel calculated from SAXS data; ϕ_{gel} corresponds to the volume fraction of gel*
 1233 *calculated from ToF-SIMS profiles of monoliths that were used to calculate the porosity of the gel formed on glass powders*

	Time (days)	Porosity (%)	pore diameter, nm	Surface area of pores, m ² /g	ϕ_{gel}
Q	180	65	4.3	451	0.05
	557	44	5	264	0.1
QCa	180	27	5.1	158	0.08
	557	9	7.5	37.6	0.19
AVM6	11	66	4.4	328	0.06
	31	47	4.5	235	0.15
	90	11	4.8	58.2	0.64

1234

1235

1236

1237

1238

1239

1240

1241

1242

1243

1244

1245

1246

1247

Highlights

- Rate-controlling vapor hydration mechanism is dependent on glass composition
- The molar ratio of $\text{Al}_2\text{O}_3/\text{MgO}$ affects glass alteration kinetics in vapor phase
- $(\text{Al}_2\text{O}_3/\text{MgO}) < 1$ seems to result in significant precipitation of Mg-smectites
- Difference between relative glass durability in aqueous medium and vapor phase
- Porosity and pore-size of altered layer is similar in the two alteration media